Sphere and Bullet Impact Cone Crack Correlation in Armour Ceramics
Master Thesis Report

by

Mick Mourmans

Submitted as part of the requirements for the degree of Master of Science
in Aerospace Engineering
at Delft University of Technology
to be defended publicly on March 16, 2026.

Student number: 6087485
Project duration: July 2025 - March 2026
Thesis committee: Dr. Y. Tang (TU Delft), Supervisor
Dr. E.P. Carton (TNO), Supervisor
Dr. S.R. Turteltaub (TU Delft), Chair
Dr. S.G.P. Castro (TU Delft), External Member

TU Delft Delft University of Technology

TNO innovation for life

Preface

This master's thesis marks the culmination of studying, prototyping, testing, optimizing, tinkering, and unforgettable times over 4.5 years of Mechanical Engineering and 2.5 years of Aerospace Engineering. Throughout internships, thesis projects, professional and less professional jobs, and especially life itself, I have found that the greatest experiences come from the people around us, for which I would like to express my gratitude to those who played an important role.

Firstly, I want to thank my thesis supervisors, Erik, Yinglu, and Prakhar, for their support, collaboration, and critical questions. Your experience and guidance have been invaluable, and I deeply appreciate the time and effort you have invested in this work. My gratitude goes out to the colleagues from TNO's ballistic research laboratory for their assistance with experiments and their solution-oriented mindset during testing.

Furthermore, I would like to thank my friends for making studying about more than just books, PDFs, and the occasional lecture, for extending academic beverages beyond coffee and late nights beyond study sessions, and for expanding my adventurous global horizons. Thank you to my housemates for the cosiness, the comfort food, the spontaneous explorations of Delft, and for bearing with ceramic tiles, tools, motorcycles, and improvised test setups scattered around the place. I would like thank all of my family for their continued support over the *"long"* academic journey, for trusting in *"Keump good!"*, and for motivating me to strive to my potential.

And ultimately, I want to thank my girlfriend, Jorijn, for her immense support, for listening to and untangling chaotic hypotheses, for her remarkable skill in supergluing and patience in assembling 3D ceramic puzzles, and for making tough times bearable and good times even more enjoyable.

This work concludes a project on a captivating topic with great potential for further research. It represents the finalization of my studies and signals the beginning of an exciting new chapter ahead as an engineer.

Mick Mourmans
March 2026

Abstract

Cone crack formation is the primary damage evolution in brittle ceramics subjected to ballistic impact. This work investigates the correlations between cone cracks generated by low velocity sphere impact and those formed under high velocity bullet impact. Al_2O_3, SiC, and Si_3N_4 ceramic tiles of varying thickness were experimentally tested for three velocity regimes (250 m/s, 300–550 m/s, 600 m/s). Macrostructural cone geometry was characterized using 3D optical microscopy and high speed imaging, mesostructural topology was evaluated through incremental R_a roughness measurements along the crack propagation, and microscopic fracture modes were quantified via SEM-based areal occurrence analysis.

Primary cone angles exhibit discrete regime-dependent plateaus achieved at transition velocities rather than continuous velocity dependence. Statistically significant inverse linear relationships are identified between primary cone angle and tile thickness, and between secondary cone angle and secondary cone height. Cone nucleation depth and minor cone radius scale proportionally with projectile radius, independent of ceramic material and velocity regime, indicating projectile-controlled nucleation geometry. Surface roughness increases progressively along the crack path for all materials and projectiles, suggesting propagation induced development of topological features. In contrast, material dependent distinct fracture modes are identified with minimal effects from projectile geometry and velocity.

Comparison between sphere and ballistic impacts reveals overlapping primary cone angle regimes, similar surface roughness amplifications, and comparable fracture modes, indicating similar crack nucleation and propagation mechanics at similar projectile velocities. Differences are primarily expressed in magnitudes of cone fragmentation and specimen recoverability for postmortem characterization of bare ceramic tiles.

In general, geometry is dominant for determining cone crack morphology, and intrinsic material properties govern microstructural fracture modes. Sphere impact testing can serve as a representative predictive screening method for understanding ballistic cone crack behaviour within defined regimes.

List of Figures

List of Tables

List of Symbols

(r, ϕ, z)	cylindrical coordinates
α	cone angle
ε	strain
$\dot{\varepsilon}$	strain rate
ν	Poisson's ratio
ρ	density
σ_c	compressive strength
σ_t	tensile strength
σ_Y	yield strength
A	surface area
AD	areal density
DoP	depth of penetration
E	Young's modulus
F	force
g	grain size
h	height
HV	Vickers hardness
K_{IC}	fracture toughness
m	Weibull modulus
M	mass
P	force
r	radius
R_a	surface roughness
t	thickness
U	energy
v	velocity
$\%_{IG}$	intergranular fracture percentage

1 Literature Research

This work on advanced ceramics touches on their origins, properties and ongoing developments, summarizes the ceramic fracture mechanisms and common testing methods, and introduces a research objective. Subsequently, ceramic cone crack terminology and characteristics, experimental and analytical research on cone cracks are presented in addition to contradicting research findings, and finally research opportunities and the research objectives of this work are discussed.

1.1 History, Characteristics, and State-of-the-Art of Armour Ceramics

1.1.1 History of Ceramics & Ceramic Armour

Humankind started manufacturing and using ceramics in the age of non-sedentary, non-agricultural hunters and gatherers at a global scale with sculpted figurines and pottery from 25000-10000 BC, with the eventual term ceramic coming from *keramikós*, a reference to Kéramos, son of Greek gods Dionysos and Ariadne and lord of the potter's district of Athens (Keramaikos).[61, 20, 20, 6, 4] The development of ceramics led, among other things, to the discovery of fired bricks for masonry (SiO_2, Al_2O_3, CaO & Fe_2O_3), glass (amorphous SiO2), glazing techniques for porcelains such as Delftware (SiO_2), tooling such as drills and cutting and machining inserts (WC), semiconductors such as LED's (GaN / SiC), rail, automotive and aircraft brakes (carbon-fibre-reinforced SiC) and aerospace turbine blade thermal barrier coatings (Y_2O_3 stabilized ZrO_2).[13, 45, 35, 63, 66, 8, 42, 28, 52]

In 1967 the Lawrence Berkeley National Laboratory experimentally found that a laminate of Al_2O_3 and aluminium was capable of stopping an armour piercing (AP) projectile travelling at 929 m/s, providing fundamental research on the ceramic armour strike face.[87] In 1969 their extensive research included reporting of fracture conoids in ceramic impact below the composite ballistic limit of different ceramics such as B_4C, BeO, SiC, SiN_3, TiB2, TiC, WC, and 6061-aluminium or fibreglass backing plates.[88] In the Vietnam war, Al_2O_3 and B_4C strike face and woven backing laminates were the first fielded protective vests for aircrew, and B_4C on aromatic polyamide fibre composite armour were the first ceramic based protection methods for helicopter seats.[30] The ceramic strike faces are adhered to metals or polymer composite backings for enhanced protection against hardened projectile threats while achieving superior areal density efficiencies compared to monolithic materials.[49]

1.1.2 Function, Chemistry, Manufacturing, and Characteristics

Lightweight and effective armour systems requires materials of low density and high resistance to penetration. The armour systems can be composed of two categories of materials; energy disruptors and energy absorbers. High strength materials, such as ceramics, are used for energy disruptors to blunt or rapidly erode an incoming projectile as kinetic energy is deflected and dispersed through fragmentation. The remaining kinetic energy is then dispersed into the absorber, such as ductile metals or fibre reinforced polymers, through plastic deformation.[32] Oxide, carbide, nitride, and boride ceramics combine covalent and ionic bonding, where shared electrons and electrostatic attraction create strong bonds, yielding rigid, undeformable and stable materials.[33] The resulting high strength, stable, and wear, corrosion and extreme temperature resistant structural ceramics are used as armour ceramics, benefiting from low density, ρ and high hardness, Hv, to provide protection against ballistic projectiles, as indicated in Table 1 for alumina, boron carbide, silicon carbide, silicon nitride, zirconia (Al_2O3, B_4C, SiC, Si_3N_4, ZrO_2) and steel.

Table 1: Mechanical Properties of Engineered Ceramics and Steel for Indicative Reference.

Material	ρ - g/cm^3	g - µm	E - GPa	ν	Hv	K_{IC} - MPa$\sqrt{m}$	σ_t - MPa	σ_c - MPa	m	Source
Al_2O_3	3.9	6	370	0.22	1478	4–5	262	2600	10	[12, 50]
B4C	2.5	15	460	0.17	2750	24	-	4343	12	[12, 50]
SiC	3.15	4	410	0.21	2800	4.0	390–450	3500	18	[12, 50]
Si_3N_4	3.16	-	320	0.26	1530	5.5	350–415	2500	20	[12, 50]
ZrO_2	6.07	1	210	0.30	1300	13	-	2500	15	[12, 50]
Steel	7.5–8	-	210–235	0.27	145–290	50–80	1110	1000–2000	90–100	[12]

Dense functional components are manufactured through sintering or reaction bonding where constituent materials or granular premixes are formed, and subsequently sintered under a combination of heat and pressure, or infiltrated by a liquid constituent for internal crystallization through capillary pressure before being machined to specification.[15, 60, 79] For ceramic coatings or intricate structures, alternative manufacturing techniques such as physical or chemical vapour deposition, plasma spraying or additive manufacturing can be employed to create unique micro- and macrostructural features and properties that provide enhanced impact or stab resistance.[10, 65, 82, 29, 17] Regardless of producing homogenous, highly dense ceramics through careful manufacturing routes, micropores are intrinsic to ceramics. The location, size and orientation of these defects govern the effects of internal stress concentrations and result in scatter of mechanical properties. The spread of stochastic fracture strength in ceramics and other brittle materials is often expressed with the Weibull exponent, m, where a higher exponent indicates increased statistical reliability.

1.1.3 State of the Art and Prospects

Modern research predominantly focusses on improving the mechanical properties and lifetime of intrinsically brittle advanced ceramics. Amongst others, the ballistic performance of advanced ceramics are improved through fractional doping of Al_2O_3 with oxides (ZrO_2, MgO, Y_2O_3)[67, 1, 51], increasing the relative density, $\rho_{\%}$, and optimizing the grain size, g, through incremental production improvements[1], transformation toughening and (continuous) fibre reinforcement, leading to the development of ceramic matrix composites,[27, 71, 62, 86] and crack deflection in structural ceramics through nano-crystalline doping and bio-inspired granular structures of ceramic composites.[55, 23, 43] Additional efforts are focussed on developing novel ceramic substances and creating multi-functional capabilities, such as radar absorbing- or (autonomous) self-healing ceramics.[19, 47, 81] Furthermore, increased computing power, the Johnson-Holmquist material model, and finite element modelling allow for simulation of the impact damage in structural ceramics that increasingly agree with experimental results .[44, 68, 80] Finally, as tightening resource availability and ecological footprint have gained global attention, ecologically friendly sources, recycling and energy responsible manufacturing routes are of key interest.[34, 31, 84, 22] These chemical, physical, structural, numerical, and environmental improvements aim at predicting, improving, retarding, deflecting and/or preventing the crack propagation of ceramics from ballistic impact.

Beyond building on the historical context, material fundamentals, and the current state of the art, the development of more advanced armour ceramics relies on deepened understanding of ceramic cracking mechanisms and fracture mechanics under ballistic impact.

1.2 Ceramic Impact Fracture

1.2.1 Ceramic Crack Mechanisms

Upon impact of a projectile on a ceramic tile both external and internal cracks form, as visualized in a section view in Figure 3, characteristic for specific material properties, impact and loading conditions. As a ceramic tile (I) gets impacted by a projectile (II) at a sufficiently high velocity, both ring cracks (III) and radial cracks (IV) become visible at the surface. Whereas beneath the surface a comminuted zone (V) forms under the impact zone, as well as median cracks (VI) through the thickness of the tile and lateral cracks (VII) spanning in-plane through the tile. Additionally, a single or multiple cone cracks (VIII) form beneath the surface of the impact face, which is the focus of this research.

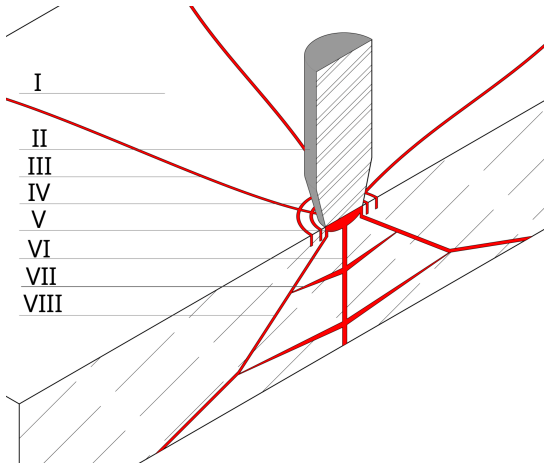

Figure 1: Visualization of Impact Induced Cracks in a Ceramic Tile (I) Cross Section. Projectile (II) Impacting from Top Down with Surface Cracks (II, III), Sub-Surface Cracks (V, VI, VII) and Formed Cone Crack (VIII).

1.2.2 Ceramic Crack Steps

For a sufficiently hard projectile with abundant kinetic energy, a ceramic tile will fracture with characteristic cracks forming in three periods:

1. The incubation period commences as the projectile touches the surface of the ceramic with deformation and erosion of the projectile, exerting compressive stresses onto the contact area. An increasing quantity and size of ring cracks develop at the surface and an increasing hemispherical comminuted zone forms beneath the surface comprised of;
   - lattice plasticity,
   - microcrack extension, and
   - microcrack coalescence and granular plasticity.
2. The formation period starts as the projectile load and micro-damage reach a critical combination, resulting in cone crack nucleation and rapid propagation through the ceramic tile as a result of multi-mode crack opening.
3. The failure period is initiated as the formed cone fully fractures from the ceramic body, while the projectile;
   - erodes the cone tip,
   - fragments the cone axially, radially and laterally, and
   - accelerates the cone and fragments

   In parallel, the perforation of the projectile through the remaining ceramic tile induces radial cracks and incrementally larger ring cracks with fine ceramic fragments.

For an insufficiently hard projectile or insufficient kinetic energy, partial fracture can occur depending on the impact and fracture mechanisms. To better grasp the progression of ceramic impact cracking and crack formation and propagation, understanding of these fracture mechanics is essential.

1.2.3 Fracture Mechanics

Impact fracture in ceramics is a complex, unpredictable balancing act of elastic- and plastic projectile deformation, ceramic fracture mechanics, micromechanical plastic deformation, depending on the crack forming period, as described in subsubsection 1.2.2, according to the steps described below.

A moving **projectile** has a kinetic energy, U_{kin}, proportional to its mass, M_p, and quadratically proportional to its velocity, v_p, as expressed in Equation 1. Upon impact with a static ceramic tile, a decelerating force, F, acts upon the ceramic tile and the projectile. This force over the impact contact area is a pressure, P, equal to the compressive stress in the projectile, σ. Initially this stress is proportional to a material's elastic modulus and strain, E and ϵ respectively, according to Hooke's law for elastic deformation (Equation 2) until the yield strength, σ_Y. For impacts beyond this strength, the contact pressure is better approximated by the dynamic pressure, p_D, which includes the density of the projectile, ρ_p, and quadratically increases with v_p, as shared in Equation 3.[11]

$$U_{kin} = \frac{1}{2} M_p v_p^2 \tag{1}$$

$$\sigma = E\epsilon, \quad if \;\; \sigma \leq \sigma_Y \tag{2}$$

$$p_D = \sigma_Y + \frac{1}{2}\rho_p v_p^2, \quad if \;\; \sigma > \sigma_Y \tag{3}$$

At sufficiently high impact velocities and sufficiently hard static ceramic targets approximations of projectile behaviour are more complicated, as plastic deformation of the projectile is accompanied with erosion through material softening, melting, and eventually fracture.

A brittle **ceramic** exhibits mostly linear behaviour until failure which enabling the use of semi-analytical models to predict failure in ceramics. Fracture in brittle ceramics is well approximated by the Griffith criterion for fracture, as it relates the energy needed to form new crack surfaces and the release in strain energy. The external stress, σ, required for extension of an existing flaw of length $2c$, for a fracture surface energy γ is calculated according to Equation 4, which is more commonly in terms of the strain energy release rate of Equation 5. Thus linking fracture of a brittle ceramic with an intrinsic critical crack length and a maximum applied tensile stress, which is derivable from a stress field.[53]

$$\sigma \geq \left[\frac{2\gamma E}{(1-\nu^2)\pi c}\right]^{1/2} \tag{4}$$

$$\frac{K_{IC}^2(1-\nu^2)}{E} \geq 2\gamma \tag{5}$$

As illustrated in Figure 2, a (spherical) projectile on a semi-infinite tile in cylindrical coordinates, (r, ϕ, z) and assuming rotational symmetry, impact is modelled process in which the static radial, tangential, and axial equilibrium equations hold, as expressed in Appendix subsection A.b. The stress field is obtained analytically from an elastic, and plastic contribution from the ceramic, given by the Boussinesq solution and a blister field (B), as expressed in Equation 6.[95, 7]

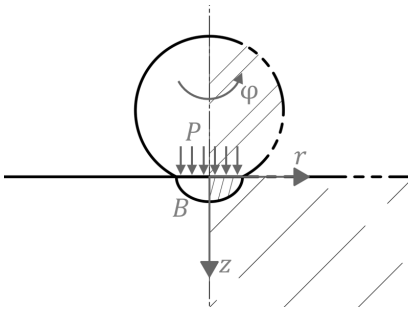

$$\begin{aligned}
\sigma_r &= \frac{P}{2\pi r^2}\left[1-2\nu-2(2-\nu)\cos\phi\right] + \frac{B}{r^3}4\left[(5-\nu)\cos^2\phi-(2-\nu)\right] \\
\sigma_\phi &= \frac{P}{2\pi r^2}(1-2\nu)\frac{\cos^2\phi}{1+\cos\phi} - \frac{B}{r^3}2(1-2\nu)\cos^2\phi \\
\sigma_z &= \frac{P}{2\pi r^2}(1-2\nu)\left[\cos\phi - \frac{1}{1+\cos\phi}\right] + \frac{B}{r^3}2(1-2\nu)(2-3\cos^2\phi) \\
\tau_{rz} &= \frac{P}{2\pi r^2}(1-2\nu)\frac{\sin\phi\cos\phi}{1+\cos\phi} + \frac{B}{r^3}4\nu\sin\phi\cos\phi
\end{aligned} \tag{6}$$

Figure 2: Illustration of spherical impact on a ceramic half-space in cylindrical coordinates (r, ϕ, z), showing the resultant projectile force (P) and the plastic/blister field intensity (B).

By examining the stress fields and plasticity, of the components of the stress tensors, shared in Equation 6, a connection is found with the crack types formed in ceramic impact, as listed in Table 2.[36]

Table 2: Ceramic Crack Formation Matrix.

	$P \leq 0$	$P > 0$
$B = 0$	-	ring cracks $(\sigma_r, z = 0)$
$B > 0$	lateral cracks $(\sigma_z, r = 0)$	radial cracks $(\sigma_\phi, z = 0)$ median cracks $(\sigma_r, r = 0)$

In the absence of plasticity ($B = 0$), the highest tensile stresses are present at the surface, $\sigma_r = P/4\pi r^2$ (z=0), forming surface ring cracks. For a small increasing positive plasticity value ($B > 0$), the polar stress along the symmetry axis dominate over the radial stress at the surface, according to $\sigma_r(z = 0) = \frac{P}{4\pi r^2} - \frac{7B}{r^3}$ and $\sigma_\phi, (r = 0) = \frac{P}{8\pi r^2} - \frac{B}{r^3}$ respectively, forming a median crack in the ceramic. For a continued increase in plasticity, the axial polar stress along the symmetry axis will become suppressed and the surface azimuthal stress will dominate, according to $\sigma_\phi(z = 0) = -\frac{P}{4\pi r^2} + \frac{2B}{r^3}$, leading to the formation of radial surface cracks. Upon removal of the load ($P \rightarrow$0) and with plasticity remaining present, the axial radial stress component becomes tensile upon unloading, $\sigma_r = P/4\pi r^2 + 2\frac{B}{r^3}$ (r=0), and a lateral cracks forms below the indentation, parallel to the surface.[36] Near the comminuted zone, a surface or sub-surface crack serve as a nucleation site for a cone crack, as expressed in Table 3.

Table 3: Cone Crack Nucleation Site Matrix.

	$P \approx B$	$20B \lesssim P \lesssim 50B$	$P \gg B$
$B = 0$	-	ring crack	ring crack
$B > 0$	median crack	comminuted zone	ring crack

For non-existent plasticity ($B = 0$), the maximum tensile principal stress, σ_1, is represented by by Hertzian indention, located just beyond the edge of the contact area, with a shallow initial crack direction relative to to the surface. For large load to plasticity ratios, i.e. $P \gg B$, Hertzian fields dominate the stress fields in Equation 6, and the σ_1 at the surface just outside the plastic zone and cone cracks can propagate from surface ring cracks. For a proportional load to plasticity ratio both greater than zero, the σ_1 lies immediately beneath the plastic zone and acts in the z-direction. At intermediate load to plasticity ratios, $20B \lesssim P \lesssim 50B$, the magnitude of the two stress fields is similar and σ_1 lies at the edge of the comminuted zone in-between the two positions described prior, with crack direction (60-90 $\circ$) varying on the position of crack initiation.[18]

1.2.4 Micro-plasticity and Inter- and Transgranular Fracture

The volume of plasticity within a ceramic impacted by a projectile, represented as B, also impacts the fracture modes of the ceramic. Plasticity in ceramics is attributed to dislocation pileups and twins generating stress along grain boundaries, followed by micro-cracking, and grain boundary sliding, which express themselves through distinct dislocation pile-ups.[83, 14] An increased dislocation density in the grains of ceramics changes a crack's path of least resistance, shifting the ceramic fracture mechanics from intergranular to transgranular fracture.[92]

The failure process of ceramics under dynamic loading is governed by intergranular and transgranular fracture mechanisms, dependent on a strain rate transition value. For a sub-critical strain rate, crack nucleation and growth are suppressed within the grains, accordingly micro-cracks propagate along grain boundaries expressed through a visibly uneven fracture surface, characterized as intergranular fracture. For dynamic strain rates above the transition rate, the strain energy release rate is sufficiently high to cause grain splitting through crack nucleation and growth, resulting in a smooth fracture surface, characterized as transgranular fracture.[85] The transgranular fracture percentage, $\%_{IG}$, is calculated from the ratio of inter- and transgranular fracture areal densities, ρ_{TG} and ρ_{IG} respectively, as described in ASTM standard C1322-15.[73]

Theoretical impact and fracture mechanics describe relationships according to ideal scenarios, whereas experimental impact aim to extract metrics and field applications may again differ from the experimental context.

1.3 Impact Testing of Ceramics

Although international test standards can classify projectile impact testing of ceramics for projectiles[56], personal body armour[37, 25, 70] and armoured vehicles[69, 24], a standardized testing method for a bare ceramic tile is non-existent and dissimilar performance metrics and analysis methods are used in literature. As listed in Table 4 and calculated according to subsection A.c, each test method has its perks and downsides, making a trade-off between bullet impact representativeness and characterization of measurable ceramic properties.

Table 4: Methods for Testing Indentation and Impact of Structural Ceramics.

Test Method	Impactor	Velocity	Advantages	Disadvantages
indentation	pyramid / sphere	<5 m/s	+ inexpensive test + standardized test + minimal ceramic damage + Hv & K_{IC} characterized + widely used in research + lab test	− (quasi-)static process − non-representative armour impact
drop test	sphere	<10 m/s	+ inexpensive test + standardized test + limited representativeness + lab test	− impact velocity limited − no ceramic properties measured − scarcely used in research − non-representative armour impact
DoP	bullet	>500 m/s	+ widely used in research + representative armour impact	− statistical variability − measurement complicated − backing required − non-standardized test − complete ceramic damage − no ceramic properties measured − shooting permit required − backing support included − yaw/spin/pitch influence
REM	bullet / sphere	>500 m/s	+ bare ceramic tested + realistic impact	− non-standardized test − analysis complicated − complete ceramic damage − no ceramic properties measured − scarcely used in research − shooting permit required
sphere impact	sphere	>50 m/s	+ inexpensive test + bare ceramic tested + widely used in research + no projectile yaw / pitch / spin + no shooting permit required + limited ceramic damage	− non-standardized test − no ceramic properties measured

Standardized **indentation techniques**, such as Vicker's or Brinell, derive the small scale plastic deformation of a material as a function of a specific indenter geometry penetrating a surface at a controlled force, enabling the calculation of a material's hardness and fracture toughness. Although commonly researched, accessible to researchers, and controllable, the tests are unrepresentative for structural ceramic behaviour under ballistic impact as the quasi-static indentation factors out the effects of dynamic impact. Additionally, spherical indenters are less suited for hard materials where a large indentation size is desired, limiting reliability with structural ceramics.

A **drop test** involves a free falling object from a set height, transforming a known potential and kinetic energy into strain energy upon impact to extract the impact shock resistance of a structural ceramic tile, with various (standardized) objects (projectiles, hammer or hardened steel ball). The benefits of commercially available lab instrumentations and standardization are to be weighed against the limited representativeness of ballistic armour bullet impact from specimen supporting or clamping effects as well as orders of magnitude smaller strain rate regimes than ballistic impact.

The depth of penetration test (DoP)[64, 90, 89] involves impacting ceramic tiles or laminates glued to a semi-infinite backing and calculating a ballistic efficiency factor from material properties and ballistic test results of a bare semi-infinite backing. Although historically widely used by military laboratories and researchers[91, 38, 16], the test method relies on large confidence intervals and has difficulties in obtaining statistically acceptable test results, which render the testing method an inaccurate and a nonconclusive metric.[9, 54]

The **residual energy method (REM)** involves a high velocity projectile impacting and penetrating a bare ceramic or laminate tile and calculating the energy absorption from the residual kinetic energy of the projectile core and cones from high speed video. This more modern testing method gives a more consistent and realistic representation of armour, but requires a high speed video and bullet catcher to reliably derive the masses involved in the perforation .

The **ball impact test** involves a hard spherical projectile impacting a bare or supported ceramic tile to analyse the damage induced in ceramics and backings at lower velocities. Lower projectile impact velocities show ceramic fracturing, with limited fragmentation, simplifying ceramic damage analysis and enabling research into crack formation. Commercially available hardened steel and ceramic spheres reduce projectile costs with symmetric impact characteristics, and can be fired with a legally purchasable gas gun, reducing the financial and legal barrier for impact testing on armour.

The described test methods are widely studied in research, whereas a complete overview of impact methods, projectiles, parameters, and the effects on cone features is key in comparing metrics and understanding the correlations.

1.4 Cone Crack Fracture Research

1.4.1 Conventions, Terminology and Bounds

To describe diverse literature definitions and conventions, this work assumes naming as visualized and indicated in Figure 3, where a ceramic tile of thickness t_c, is impacted by a projectile of radius R_p, where at a projectile contact radius r_p a cone is formed of minor radius r_c, major radius R_c, cone height h_c and a related cone angle α. The projectile and cone velocity and mass, M_p, v_p, v_p^*, M_c, and v_c, are equal to those mentioned in Appendix/subsection A.c Additionally, cylindrical polar coordinates, (r, ϕ, z), is conventional with the origin at the impact centre, radial distance (r) in the ceramic plane, azimuth (ϕ) rotational symmetry assumed around the main axis, and height (z) defined in the direction of projectile velocity.

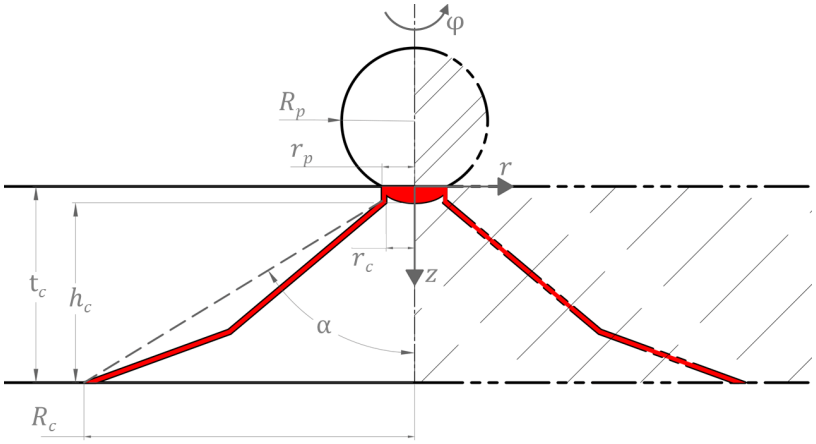

Figure 3: Visualization of Cone Crack and Terminology in a Ceramic Tile Impact Section.

Select research defines minor and major angles for the cone crack separately[80, 94, 96], however in this work a single continuous α is assumed according to Equation 7, calculated in Appendix/subsection A.a, as R_c is assumed constant (i.e. equal pressure distribution to armour backing), and this convention allows for convenient correlation with existing literature, and fractured cone angle measurement from high speed videography.

$$tan(\alpha) = \frac{R_c - r_c}{h_c} = \frac{-3r \pm \sqrt{\frac{12V}{\pi h} - 3r^2}}{2h} \tag{7}$$

Additionally, as multiple cones can form during ceramic fracture, as explained in subsubsection 1.2.1, only the principle fractured cone is investigated. Impact velocity research and analysis is limited ($\approx$ 50 - 1000 m/s) to stay within realistic range for cone crack formation and ballistic range of bullets.

1.4.2 Experimental Research on Cone Cracks

The correlations found in experimental work on cone crack geometry, as summarized in Table 5, are discussed and compared.

Early experimental research is performed by **Field**, Sun and Townsend on the impact of a hardened steel sphere (R_p = 2.5 mm) on glass ceramics and Al_2O_3 tiles over a wide velocity range ($50 < v_p < 900$ m/s).[26] Their analysis indicated that the Al_2O_3 cone angle increases as the velocity increases, $\alpha_{220m/s} < \alpha_{800m/s}$, and linked this to fragmentation of the projectile and the material flow modifying the stress field, whereas the authors indicated a glass ceramics cone angle decrease for higher velocity impacts, $\alpha_{40m/s} > \alpha_{90m/s}$, attributed to an expanding projectile contact radius, r_p, during impact. The authors attributed roughness of the cone surface to the amplitude of stress wave reflected in the ceramic, which directly correlates with the projectile impact velocity. Additionally, the relative hardness of the projectile and tile specimen is regarded of great importance to the elastic- and plastic energetics of impact, whereas the ceramic toughness is regarded as sub-significant.

More recent work by **Khan** et al. on hardened steel bullets (R_p = 5.45 mm) impacting 5 mm thick Al_2O_3 tiles at lower velocities ($50 < v_p < 275$ m/s) indicates a similar trend to Field et al., where higher impact velocities yield greater cone angles, $\alpha_{52m/s} < \alpha_{275m/s}$, with significant variation between measurements.[40] It was found that an increase in projectile velocity lead to a greater quantity of radial and ring cracks and the formation of finer ceramic fragments.

Recent work by **Yuan** et al. on high speed (274-1040 m/s) impact of spherical 304 stainless steel projectiles (R_p = 2.5 mm) on 10 mm thick Al_2O_3 tiles, found that cone angles increase as the impact velocity rises, $\alpha_{274m/s} < \alpha_{1040m/s}$.[96] These results are geometrically linked, as per Equation 7, to a decrease in h_c, attributed to ceramic granulation and cone erosion, and to an increase in R_c, reportedly from an increase in projectile deformation. Cone fracture is linked to splitting due to spallation and finally fragmentation, observing more pronounced transgranular fracture, decreased observance of microporosity and microplastic deformation near the impact point for intermediate to higher velocities (488, 802 & 1040 m/s respectively).

Akimune tested steel and yttria-stabilized zirconia, YSZ, spherical projectiles (R_p = 0.4 mm) impacting a 3 mm thick SiC tile at low velocities.[3] Sub surface cone angles were locally measured near the impact area from a polished section of the impact site and related to the impact velocity, and deformation behaviour of the sphere and target material. Generally, smaller cone angles are reported for higher projectile speed, $\alpha_{100m/s} > \alpha_{270m/s}$, acclaimed to be from different Hertzian stress field trajectories. For dissimilar projectile materials a greater cone angle, $\alpha_{ZrO_2} > \alpha_{steel}$, was found for greater projectile hardness $Hv_{ZrO_2} > Hv_{steel}$, attributed to lower projectile deformation. The author observed a greater quantity of nucleated non-aligning cone cracks for an increasing degree of projectile penetration, where the response behaviour and contact behaviour proceed from the ratio of target to projectile hardness, Hv_c/Hv_p.

Toussaint and Polyzois experimentally impacted Al_2O_3 tiles of different thickness at various velocities with E52100 chrome steel spherical projectiles (R_p = 3.175 mm) for calibration of a ceramic model.[80] The cone angle for thin Al_2O_3 tiles (9.1±0.3 mm) marginally (< 2%) decreases for an increasing impact velocity, $\alpha_{100m/s} > \alpha_{300m/s} > \alpha_{500m/s}$, calculated from R_c through Equation 7. For thicker Al_2O_3 tiles (13.2±0.3 mm) the cone angle, calculated similarly through Equation 7, remains approximately equal for lower and higher velocity ranges, $\alpha_{200/s} \approx \alpha_{800m/s}$. On average the cone angle is smaller for the thicker tiles relative to the thinner tiles for various projectile velocities, $\alpha_{9mm} > \alpha_{13mm}$. Moreover, the authors uniquely distinguished cone crack fracture surfaces according to the terminology of ASTM C1322[73]. For 13 mm tiles at intermediate impact velocities (200-499 m/s), the fracture surface progresses from a smooth *mirror finish* near the comminuted zone, to a *mist fracture* with medium roughness and a cone-angle shift, and ultimately to a rough *hackle fracture* with a sharp angle change near the rear.

Kedir et al. experimented with larger spherical steel, partially stabilised ZrO_2 and Si_3N_4 projectiles (R_p = 0.75 mm) impacting 3 mm thick SiC at intermediate velocities (200-340 m/s), with all findings in agreement with prior experimental work.[39] Smaller cone angles were observed for greater ZrO_2 projectile impact velocities, $\alpha_{ZrO_2\text{-}216m/s} > \alpha_{ZrO_2\text{-}320m/s}$, but similar cone angles were observed for Si_3N_4 projectile impact velocities, i.e. $\alpha_{Si_3N_4\text{-}216m/s} \approx \alpha_{Si_3N_4\text{-}320m/s}$. Greater cone angles $\alpha_{Si_3N_4} > \alpha_{ZrO_2} > \alpha_{steel}$ were observed for harder projectiles $Hv_{Si_3N_4} > Hv_{ZrO_2} > Hv_{steel}$, attributed to reduced projectile deformation and hence smaller r_p.
, with all findings in agreement with prior experimental work[3, 72]. Through synchrotron X-ray radiography of the projectile impact, a two-dimensional projection of the fracture volume reveals the formation of a sub-surface cone crack within the first microsecond after impact, prior to complete projectile deformation/cracking/pulverization and prior to the formation of other ceramic cracks. Additionally, the authors consistently observe predominantly transgranular fracture at all cone fracture surfaces, with slightly greater intergranular fracture at a greater distance from the impact location, regardless of projectile material.

Ma et al. conducted research on impact of thick Q235 steel cylindrical projectiles (R_p = 10.8 mm) on Al_2O_3 tiles (t_c = 8,12,15 mm) with a Q235 steel backing (8 mm) and a Kevlar crack-arresting layer (0.5 mm) adhered to the ceramic strike face.[48] For 8 mm tiles, a drop in cone angle is observed for lower impact velocity, however the cone angle is independent of velocity at faster impact velocities, $\alpha_{162m/s} > \alpha_{218m/s} \approx \alpha_{404m/s} \approx \alpha_{518m/s}$. A similar trend is observed for 12 mm and 15 mm tiles, where $\alpha_{323m/s} \approx \alpha_{427m/s} \approx \alpha_{518m/s}$ and $\alpha_{321m/s} \approx \alpha_{414m/s} \approx \alpha_{541m/s}$ respectively. For the intermediate and high velocity impacts (218-541 m/s) the cone angle is reported to be related to the ceramic thickness with a maximum cone angle for 12mm Al_2O_3 tiles, i.e. $\alpha_{8mm} < \alpha_{12mm} > \alpha_{15mm}$.

Research by **Leavy**, Brannon and Strack included ballistic impact experiments on thick SiC and B_4C ceramics cylinders ($\varnothing = t_c = 25.4$ mm) with WC sphere projectiles ($R_p = 3.175$ mm) at velocities between 50 and 500 m/s.[46] For an increasing impact velocity, the cone angle decreases, and the quantity of cone cracks increase substantially, with no indication of dissimilar behaviour between the ceramic materials. Utilising X-ray computed tomography analysis allowed the authors to non-destructively reconstruct a 3D map that enables 360°measurement of the major cone crack.

Yang et al. investigated cone cracking in Al_2O_3 tiles of 5, 8, 10 and 12 mm thick at by impact of Q235 steel spheres ($R_p = 5$ mm) at intermediate impact velocities (230-400 m/s).[94] Their findings suggest that cone angles are inversely related to ceramic tile thickness, such that for comparable impact velocities ranges $\alpha_{5\text{mm}} > \alpha_{8\text{mm}} > \alpha_{10\text{mm}} > \alpha_{12\text{mm}}$. Additionally, they observed a reduced thickness or rise in impact velocity significantly increase cone fragmentation and ceramic tile spallation.

Oh et al. experimentally researched cone cracks formed in 4 mm SiC tiles by impacting 1.2 and 2.0 mm SiC and steel spheres of different sizes in the range of 30-250 m/s.[58] Moderate negative correlations between cone angle and impact velocities are reported, with steeper trends for steel spheres than for SiC spheres ($(-\Delta\alpha/v_p)_{SiC} > (-\Delta\alpha/v_p)_{steel}$), attributed to a difference in material density, and steeper trends for larger spheres than smaller spheres $(-\Delta\alpha/v_p)_{2.0mm} > (-\Delta\alpha/v_p)_{1.2mm}$. Furthermore, an empirical equation for the cone angle was obtained for the cone from the particle and tile density, impact velocity and projectile radius.

Extensive research efforts by **Yamada** et al. on impact testing a range of 4 mm thick bare ceramics (B_4C, Al_2O_3 of several purities and sintering temperatures, ZrO_2, Si_3N_4, Al_2O_3/ZrO_2 & Al_2O_3/SiO2) at an approximately constant 320 m/s with SUJ-2 steel spherical projectiles ($R_p = 0.5$ mm).[93] Although sintered according to similar sintering temperatures (≈1600 °C), for an increased Al_2O_3 purity a negative correlation with the cone angle and an increase in intergranular fractures are observed, i.e. $\alpha_{\text{A96}} > \alpha_{\text{A99}} > \alpha_{\text{A99.99}}$ calculated according to Equation 7. For equally pure Al_2O_3 tiles (A99.99) sintered at dissimilar sintering temperatures (1350, 1450 & 1600 °C) a similar trend is apparent, where a higher sintering temperatures inversely correlates with cone crack angle, such that $\alpha_{1350°\text{C}} > \alpha_{1450°\text{C}} > \alpha_{1600°\text{C}}$. Most noticeably, a clear correlation was found between larger cone cracks forming for materials with lower fracture toughness, where: $\alpha_{\text{Al}_2\text{O}_3/\text{SiO2}} > \alpha_{\text{B}_4\text{C}} > \alpha_{\text{A99}} > \alpha_{\text{Si}_3\text{N}_4}$ and similarly $K_{IC-\text{Al}_2\text{O}_3/\text{SiO2}} < K_{IC-\text{B}_4\text{C}} < K_{IC-\text{A99}} < K_{IC-\text{Si}_3\text{N}_4}$. This finding equally holds for the collection of Al_2O_3 tiles discussed prior, however not for the ZrO_2 and Al_2O_3/ZrO_2 tiles, allegedly due to ZrO_2 stress-induced phase transformation (a transformation toughening mechanism as described in subsubsection 1.1.3). Furthermore, analysis of the main fracture modes indicated a greater ratio of trans- to intergranular fracture, $\%_{gfrac}$ as calculated through **??**, for ceramics with lower K_{IC} and higher α, but a lower percentage of kinetic energy consumed by fracturing. Different materials and sintering temperatures are presented, influencing grain nucleation and growth which are not quantified or controlled in the research, but most likely play a significant role in inter- and transgranular fracture modes and micro scale fracture mechanics.

Table 5: Experimental Correlation of Cone Angle Parameters, Extracted from Reported Data.

Publication	Projectile				Ceramic		Correlation	
	[A]	[B]	[C]	[D]	[E]	[F]		
Akimune, Y., 1990	●	0.8	CrSt YSZ	100-270	SiC[a]	3	$\alpha \propto -v_p$ $\alpha \propto Hv_p$	[3]
Field et. al., 1989	●	5	HSt	32-402	glass ceramics	≈10	$\alpha \propto -v_p$	[26]
				50-900	Al_2O_3	≈10	$\alpha \propto v_p$	
Kedir et al., 2021	●	1.5	Si_3N_4 YSZ CrSt	256-339 211-320 316	SiC[a]	3	$\alpha \propto -v_p$ $\alpha \propto Hv_p$	[39]
Khan et al., 2020	▬►	10.9	HSt	52-275	Al_2O_3	5	$\alpha \propto v_p$	[40]
Leavy et al., 2010	●	6.35	WC	50-500	SiC[a] B_4C[a]	25.4	$\alpha \propto -v_p$	[46]
Ma et al., 2025	▬	10.8	St	162-541	Al_2O_3	8-15	$\alpha \not\propto v_p$ $\alpha \propto t_c$	[48]
Oh et al., 2005	●	1.2 2.0	SiC St	30-250	SiC[a]	4	$\alpha \propto -v_p$ $\alpha \propto -r_p$ $\alpha \propto -\rho$	[58]
Toussaint et. al., 2019	●	6.35	CrSt	100-832	Al_2O_3	9 13	$\alpha \not\propto v_p$ $\alpha \propto -t_c$	[80]
Yamada et al., 2010	●	4	CrSt	320	Al_2O_3[b] Al_2O_3/SiO2 Al_2O_3/ZrO_2 B_4C Si_3N_4 ZrO_2	4	$\alpha \propto -K_{IC}$ $\alpha \propto \%_{gfrac}$	[93]
Yang et al., 2024	●	6	St	217-409	Al_2O_3	5-12	$\alpha \propto -t_c$	[94]
Yuan et al., 2025	●	5	SS	274-1040	Al_2O_3	10	$\alpha \propto v_p$ $h_c \propto -v_p$	[96]

[A]: Projectile geometry (●: sphere, ▬►: bullet, ▬: cylinder)
[B]: Major projectile diameter - mm
[C]: Projectile material (St: steel, CrSt: chrome steel, HSt: hardened steel, SS: stainless steel, YSZ: Yttria stabilized Zirconia, WC: Tungsten Carbide)
[D]: Impact velocity range - m/s
[E]: Ceramic material
[F]: Ceramic thickness range - mm
a: Ceramic tile supported by backing.
b: Alumina of 96/99/99.99 $\%_\rho$, with 99.99 $\%_\rho$ sintered at 1300/1450/1600 °C.

1.4.3 Analytical Research on Cone Cracks

Analytical approximations of the cone angle are listed in Table 6, analysed and discussed.

Table 6: Analytical Correlation of Cone Angle Parameters.

Publication	Correlation	
Kobylkin, I.F., 2017	$\alpha = f(t_c, r_p)$ $\alpha = f(\sigma_c, \sigma_t)$	[41]
Oh!		
Yang et. al., 2024	$\alpha = f(K_{IC})$ $\alpha = f(\sigma_t)$	[94]

An analytical formulation has been formed by Kobylkin for a cylindrical projectile onto a ceramic tile, by stating that the minimal force required to cut a conical surface must be greater or equal to the force required to shear a cylindrical plug.[41] The analytical formula for the cone angle, as expressed in Equation 8, becomes a function of geometric parameters, t_c and r_p, and ceramic strength, σ_c and σ_t, where an increase in compressive over tensile strength yields a smaller cone angle, and a greater ceramic thickness over projectile radius yields a lower cone

angle.

$$\tan\alpha = \frac{r_p}{4t_c}\left[-\left(1+0.5\frac{2t_c}{r_p}\right) \pm \sqrt{\left(1+0.5\frac{2t_c}{r_p}\right)^2 + 8\frac{t_c}{r_p}\left(\frac{1}{\sqrt{3}}\frac{\sigma_c}{\sigma_t} - 0.5\right)}\right] \tag{8}$$

Semi-analytical work by Yang et al. has utilized fitting of experimental data of ceramic tiles impacted by spherical projectile to numerically find a minimum sum of cone fracture energy and deformation energy.[94] Through parametric analysis it was found that an increase in either fracture toughness or tensile strength yields a significantly decrease in cone angle. For greater resistance of the ceramic material to crack formation and propagation, less energy gets converted to ceramic fracture energy, ultimately decreasing the cone angle.

1.4.4 Discussion and Opportunities

Although a lack in consistent reporting of ceramic microstructures, defects and analysis methods is evident and no direct comparisons can be made between experimental works, the discrepancies in correlations indicate uncertainties and research gaps within the research field. As expressed in subsubsection 1.2.3, Table 5, and Table 6 respectively, fracture mechanics theory, experimental research, and analytical research have illustrated a handful of functions for various cone crack angle:

Fracture Mechanics Theory :	$\alpha = f(\ P\ ,\ B\ )$
Experimental Research :	$\alpha = f(\ v_p\ ,\ t_c\ ,\ Hv_p\ ,\ K_{IC}\ ,\ \%_{gfrac}\ )$
Analytical Research :	$\alpha = f(\ r_p\ ,\ t_c\ ,\ \sigma_c\ ,\ \sigma_t\ ,\ K_{IC}\ )$

The contradictory correlations found in literature between cone angle and projectile velocity indicate a key uncertainty for the research question at hand, therefore requiring additional and more focussed experimental work. The effects of geometric parameters on the cone crack angle align with the complexity of the fracture mechanics for both projectile and ceramic. Where care is to be taken to avoid interconnectivity with impact parameters for future research.

Inconsistencies and contradictions are partially attributed to a lack of a measurement standards for impact testing, cone descriptions and characterization methods, and investigated material properties in the experimental research. The cone angle is differently measured amongst different researchers, where multiple nested or secondary cones cones have rarely been reported. Investigations into 2D cone angle only at the surface, complete cones without secondary angles, or cone volume are described differently and are non-descriptive and non-comparable.[3, 39, 26, 93] Research commonly mistakes surface nucleated cones, as formed in Hertzian contact mechanics, and sub-surface nucleated cones, as formed in high speed impact and assume similar fracture mechanic behaviour. Secondary crack formation and roughness increase are sometimes attributed to internal stress-wave interactions, or crack formation at the rear of the tile, which contradict traditional ceramic fractography and the reported crack initiation near the impact point within 1.5 microsecond.[field, 39] Analytical work formulating a cone angle as a function of geometric and intrinsic ceramic properties has rarely been compared to experimental research and relies on precise characterization of the tensile strength of ceramics, which is rarely measured and rather a measure of the greatest sizes present in the ceramic.[field, 39, 59] Additionally, the statistical behaviour of dynamic projectile impacts on ceramics are scarcely discussed in research, thereby not accounting for the inherent statistical nature of ceramics and the variance in the dynamic impact process. Although the prior focus of ballistic ceramics developments has been on toughening the materials to prevent fracture, both experimental and analytical work indicate an inverse relationship with cone angle formation, and consequently impact energy disruption. This creates opportunities of investigating the energy disrupting capabilities of tailored ceramics, and additionally, the mentioning of the ratio of inter- and transgranular fracture modes in various materials opens up possibilities for further research into distinguishing micro plasticity induced crack nucleation and strain rate dependent crack propagation.

The presented literature research includes experimental work explicitly on cone crack formation, analytical research explicitly on cone crack formation, and highlighting of uncertainties, contradictions, and shortcomings in existing research to ultimately identify novel research opportunities and analytical formulations as the foundation of a research proposal. As cone angle has been studied for sphere impacts, no research has been done

on the relationship between sphere impact at low velocities and bullet impact higher velocities – it was merely assumed.

1.5 Research objective

The fracturing of ceramic materials by impact of a small steel sphere avoid the fragmentation from bullet impacts, while yielding a cone crack and enabling easier reconstruction and characterization of cone geometry, crack propagation, and fracture modes, subsequently allowing more convenient prediction of the ballistic performance of ceramics.

The research objective of this work is to analyse the correlation between the cone cracks formed by low velocity sphere impact testing and those formed in high velocity bullet impact testing.

This research question is decoupled into geometric and testing variables, intrinsic ceramic properties, and aims at methodically finding correlations through three sub-research questions:

1. How do impact geometry and velocity affect the cone crack morphology and fracture mechanics?
2. How do intrinsic ceramic properties affect cone crack morphology and fracture mechanics?
3. Can sphere impact predict bullet impact cone crack morphology and fracture mechanics?

To answer these questions, projectiles and ceramics are gathered, impact testing is planned, characterization methods are identified and analysed, and the results are presented, analysed for statistical ground and eventually compared to for low velocity sphere impact and high velocity bullet impact.

2 Methodology

2.1 Materials

A selection of ceramic tiles and projectiles is assembled and characterized, focussing on introducing variation in ceramic properties while maintaining projectile characteristics, subject to material availability, with detailed measurement settings and derived properties expanded on in Appendix B.

A collection of alumina, Al_2O_3, silicon carbide, SiC, and silicon nitride, Si_3N_4, ceramic tiles are characterized, as listed in Table 7. Material density, ρ, is measured using a digital micrometer and precision scale. Chemical composition is verified through energy-dispersive spectroscopy (EDS) and the average grain size, g, is determined by analysis of scanning electron microscopy (SEM) images, as per ASTM standards E1508 and E112 respectively.[77, 75] The elastic modulus, E, and poisson ratio, ν, are derived from the material sonic velocity as measured according to ASTM E494.[78] The Vickers microindentation hardness, HV, is characterized according to ASTM C1327 and the Niihara-Palmqvist fracture toughness, K_{IC}, is derived.[74, 57]

Table 7: Ceramic Tile Materials and Characterized Properties.

	ρ - g/cm^3		g - µm	E - GPa		ν		HV		K_{IC} - MPa m$^{1/2}$	
Material	μ	σ		μ	σ	μ	σ	μ	σ	μ	σ
Al_2O_3	3.865	±0.016	6.5	356	±4	0.224	±0.012	1679	±139	4.18	±0.25
SiC	3.173	±0.037	1.9	423	±20	0.155	±0.007	2875	±133	4.27	±0.28
Si_3N_4	3.216	-	2.9	289	-	0.268	-	1610	±57	8.40	±1.37

μ = mean value; σ = standard deviation

The projectiles include bearing balls with diameters of 4.5 and 5.35 mm, and 7.62 x 51 P80 armour-piercing bullets, as visualized in Figure 4 and listed in Table 8.

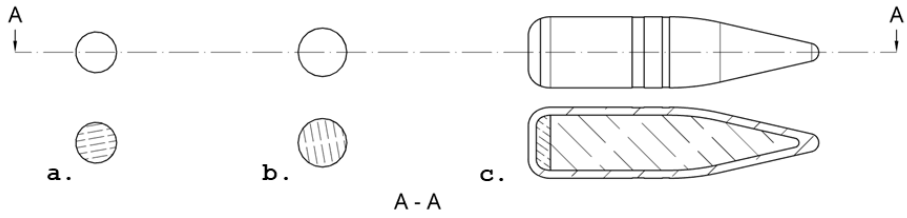

Figure 4: Schematic of Projectiles and Cross Section for Experimental Research: 4.5 mm Sphere (a.), 5.35 mm Sphere (b.) and 7.62 x 51 P80 Bullet (c.) with Jacket, Steel Core and Lead Core.

The physical diameter mass and density, $\emptyset$, M and ρ, of the spheres are measured using a digital micrometer and precision scale. The material compositions are determined by energy-dispersive spectroscopy (EDS) in accordance with ASTM E1508 and Vickers hardness, HV, is measured according to ASTM C1327.[77, 74] Physical and material properties of bullets are derived from a technical report with hardness values are converted according to ASTM E140.[21, 76]

Table 8: Projectile Materials and Characterized Properties.

		$\emptyset$ - mm		M - g		ρ - g/cm^3		HV	
Projectile[1]	**Material**	μ	σ	μ	σ	μ	σ	μ	σ
●	Bearing steel (Fe-1.5Cr-0.3Mn)	4.50	±0.01	0.372	±0.001	7.80	±0.01	969	±15
❍	High carbon Fe-based steel	5.35	±0.01	0.625	±0.001	7.80	±0.01	1093	±33
jacket	Brass (Cu-10Zn)	7.82	-	-	-	-	-	142	±2
▬► **St core**	Low-alloy Cr steel (Fe-1.9Cr)	6.15	±0.01	3.950	±0.06	-	-	849	±31
Pb core	Lead	-	-	-	-	-	-	-	-

μ = mean value; σ = standard deviation

[1]: Projectile geometry (●: 4.5 mm sphere, ❍: 5.35 mm sphere, ▬►: 7.62 P80 bullet)

2.2 Impact Test Methods

Two projectile impact test methods are used for different projectile types and described below. Tests are performed at TNO's Laboratory of Ballistic Research (LBR) in climate controlled indoor firing ranges.

2.2.1 Sphere Impact Test

For testing the impact of 4.5 and 5.35 mm spherical projectiles on ceramic tiles a gas gun is used, as schematically represented in Figure 5. Ceramic tiles are cut into 50 x 50 mm squares using a diamond saw to increase the available test data and the edges of each tile are taped with a flexible PVC insulation tape for facilitation of post-impact tile reconstruction.

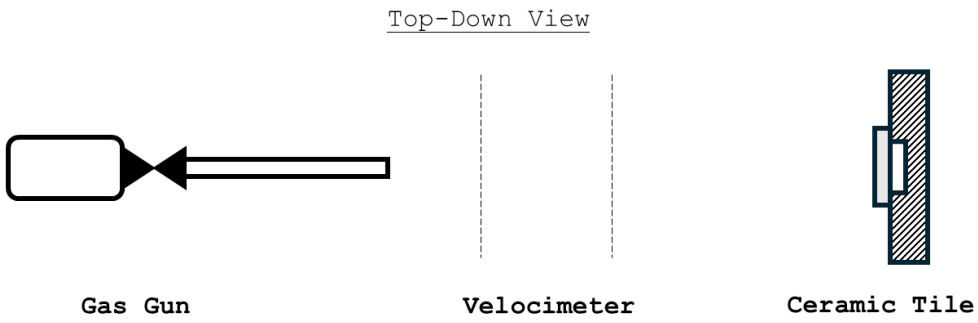

Figure 5: Schematic of Air Gun Impact Test Setup.

ballisticresearch A gas pressure accelerator, supplied by Ballistic Research[5], is used for shooting the spherical projectiles at the ceramic tiles. The gas gun is positioned 1.5 m from the target with an intermediate 2-gates light velocimeter. A combination of a 5.4 mm barrel (285 or 1200 mm) accelerating gas (N_2 or He) and pressure ($\leq$ 180 bar) are established and tuned to reach a desired projectile velocity up to 700 m/s. Ceramic targets are simply supported by positioning on a ledge and negligibly constrained, with a 45 mm diameter hole and soft padding at the rear surface to catch cone fragments.

2.2.2 Bullet Impact Test

For impact testing of armour-piercing bullets on ceramic tiles a gun barrel is mounted in a breach and aimed at a 100 x 100 mm ceramic tile with a 2-gates light velocimeter in the bullet trajectory, as visualized in Figure 6.

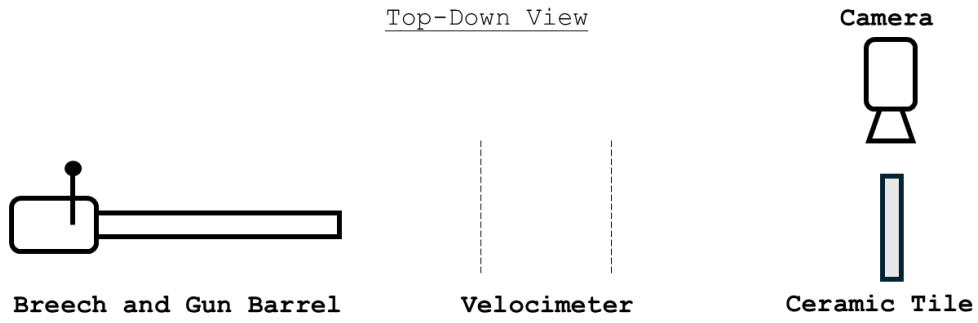

Figure 6: Schematic of Bullet Impact Test Setup.

A PROTOTYPA UZ-2002 Universal ballistic breach is used, as per NATO AEP-97 standard, and a 0.5 MHz Shimadzu HyperVision HPV-2 high speed camera is positioned from the side of the tile and is digitally triggered by the velocimeter.[2] The ceramic tile is positioned upright, unsupported on a ledge and manually aligned for minimal obliquity.

2.3 Cone Characterization

The macrostructural, mesostructural and microstructural features of cone fragments are characterized through various measurement and analysis techniques with distinct derivations listed in Table 9 and detailed measurement settings in Appendix B.

Table 9: Characterized Features at Investigated Length Scales, with Derivation Digital Microscopy, High Speed Video (HSV), and Scanning Electron Microscopy (SEM).

Scale	Symbol	Features	Derivation	Unit
	α	angles of cone surfaces	3D reconstruction, HSV and aligning	°
macro	r	radius of cone features and transitions	3D reconstruction, HSV and marking	µm
	h	height of cone features and transitions	3D reconstruction and marking	µm
meso	R_a	surface roughness over cone perimeter	3D reconstruction and line measurement	µm
micro	$\%_{IG}$	intergranular fracture ratio	SEM and microstructure identification	-

2.3.1 Macrostructural Characterization

For measurements of geometric cone features on a macrostructural scale 2D and 3D image stitching and high speed video analysis are employed.

For sphere impacted tiles, the formed cone and tile crater are respectively 3D mapped and 2D photographed under an OLYMPUS DSX-1000 digital microscope. In-plane image views of the cone and crater are used to measure minor cone radius, r_1, and major cone radius, r_4, as illustrated in Figure 7. Section views of the 3D cone are used to extract cone height, h_1, primary and secondary cone angles, α_1 and α_2, and cone angle transition locations, r_2, h_2, r_3 and h_3, as visualized in Figure 8.

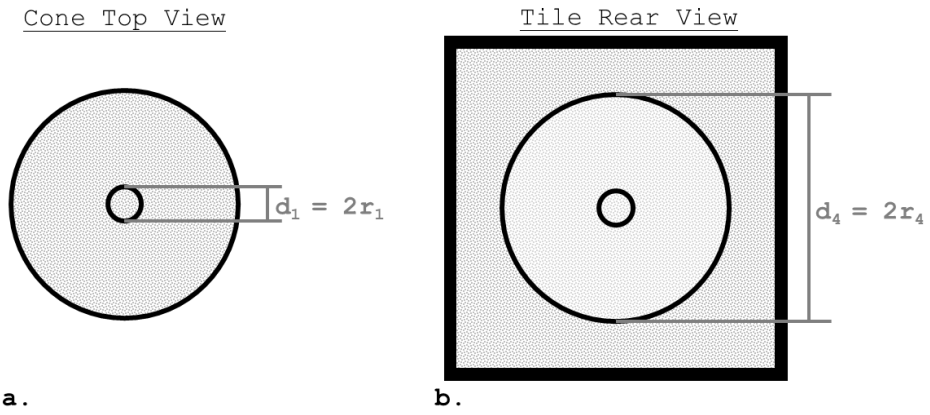

Figure 7: Schematic of Digitally Reconstructed Cone (a.) and Tile (b.) with Measured Minor and Major Cone Crack Radius.

For bullet impacted tiles, the remnants of the tile are 2D photographed under an OLYMPUS DSX-1000 digital microscope and the high speed video images are analysed. The major cone radius, r_4, is measured from the high speed video from the fracture cloud plumes generated at the rear of the ceramic tile and cross-checked with the imprint from the 2D image. Subsequently cone angles, α_1, are calculated from the plume radii, projectile radius and tile thickness, r_n, r_p, and t_c, as expressed in Equation 9.

$$\alpha_1 = \arctan\left(\frac{r_n - r_p}{t_c}\right) \tag{9}$$

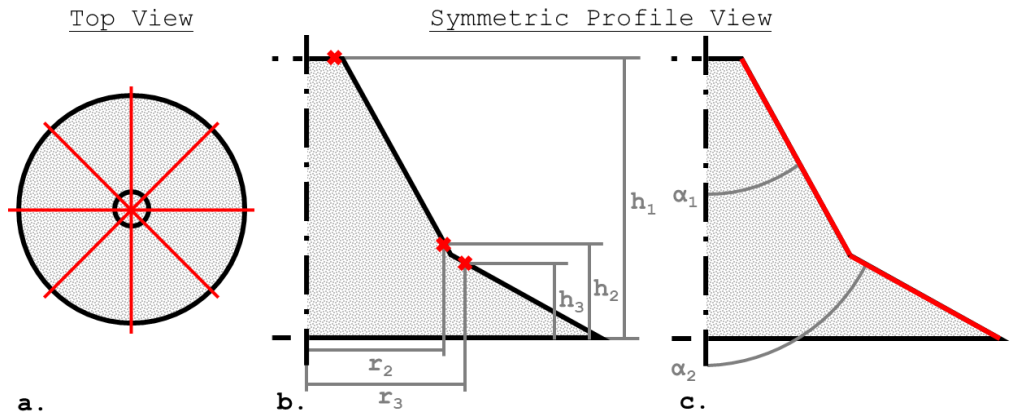

Figure 8: Schematic of Digitally Reconstructed Cone (a.) and Section Views (b.-c.) with Measured Cone Heights and Radii and Primary and Secondary Cone Angles with respect to Central Axis.

2.3.2 Mesostructural Characterization

Mesostructural texture features are characterized through roughness measurements of the 3D reconstructed cones and tiles.

As visualised in Figure 9, five equally spaced line measurements are performed over the perimeter of the cone and tile surface forsphere and bullet impact respectively, and the mean arithmetic profile roughness, R_a, calculated the from the height deviation, $h(x)$, over the line measurement length, l_r according to Equation 10.

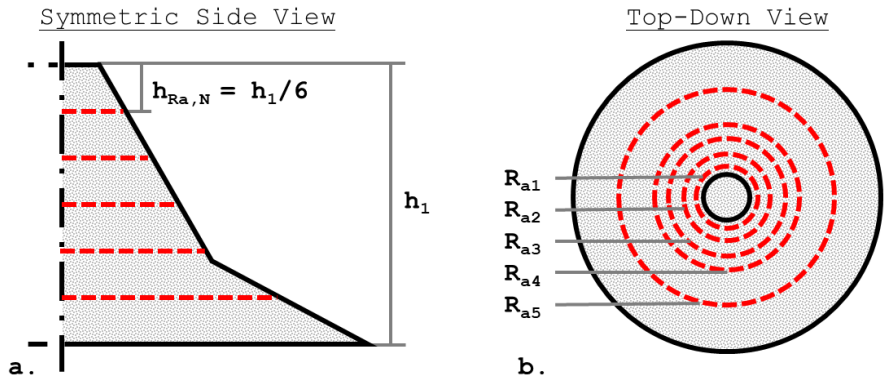

Figure 9: Schematic of Mean Arithmetic Surface Roughness Line Measurements From an Incremental Height Perspective (a.) and in Numbered Order (b.).

$$R_{aN} = \frac{1}{l_r} \int_0^{l_r} |h(x) - h_{Ra,N}| \, dx \tag{10}$$

2.3.3 Microstructural Characterization

A selection of cone crack fracture surfaces are examined under a scanning electron microscope (SEM) to better understand the crack formation and propagation mechanisms at play, in accordance with steps described by ASTM C1233.[73]

Cone specimens are investigated in a JEOL JSM-7500 at x25, x100, x500, x2000 and x5000 magnification. At each magnification the cone is imaged from the one top view, and five views equally distributed locations along the cone crack propagation. Visual characteristics are noted, marked in the image, and a relative areal

occurrence density is defined and linked to ceramic fracture modes, as listed in Table 10 and visualised in Figure 10.

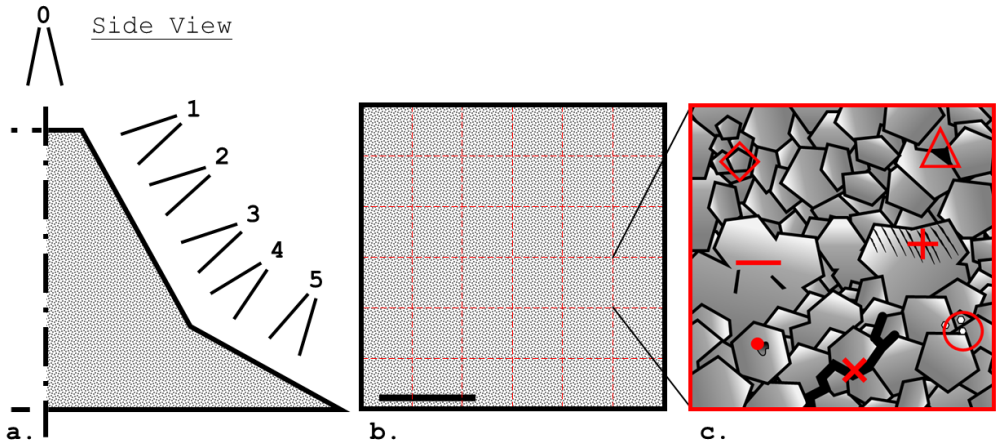

Figure 10: Schematic of Fracture Surface Inspection Locations (a.), SEM Image and Areal Subdivision (b), and Fracture Microstructure and Visual Marks (c.), as Listed in Table 10.

Table 10: Classification of Ceramic Fracture Modes and Associated SEM Visual Markers.

Fracture Mode	Visual Marks	Image Marker
Intergranular	Exposed geometric grain boundary	◇
	Triple junction pores	△
Transgranular	Flat fracture planes	−
	Cleavage marks (Striations / hackles / micro-steps)	+
Secondary damage	Micro-pores / dimples	·
	Secondary cracks	X
	Micro particulates	○

2.4 Experiment Matrix

To answers the research questions, the projectile geometry, diameter, and velocity as well as ceramic tile thickness and materials are selected as dependent variables, presented in Table 11. The tile length and width, impact aiming location and the absence of a backing are kept constant as control variables. Ambient temperature, humidity, projectile yaw, and tile edge distance are recorded during impact tests, but are treated as extraneous variables. Ceramic ageing and residual stresses as well as projectile spin are considered confounding variables for their lack of control during testing.

Table 11: Experimental Test Matrix for Impact Testing of Structural Ceramics.

Ceramic Tile		Projectile[A]		
Material	mm	≤ 343 m/s	343 - 550 m/s	≥ 550 m/s
A - Al2O3	7.8	● ❍		
	10	● ❍	● ❍	❍ ▬►
	12			▬►
	14	❍	● ❍	
	20		❍	▬►
C - SiC	7.8	●		▬►
	8.15	❍		
	12	●	●	
H - Si3N4	7.2	●	●	▬►

[A]: Projectile geometry (●: 4.5 mm sphere, ❍: 5.35 mm sphere, ▬►: 7.62 P80)

3 Results

This section presents the results of the experimental impact testing and subsequent cone characterisation at the macro-, meso-, and microscale. Observed trends are analysed systematically, regression models are statistically evaluated, and relationships between experimental factors and cone responses are examined in relation to the research questions. Ultimately, the interpretation of the results form the foundation for formulating predictive insights between cones produced from sphere and bullet impacts.

3.1 Impact Test Outcomes

The series of experiments with combined factors of projectile type, projectile impact velocity, v_p, ceramic material and tile thickness, t_c, resulted in either no cone formation, a single cone, or multiple nested cones detached from the ceramic tile, as visualized in Figure 11 and illustrated in Figure 12.

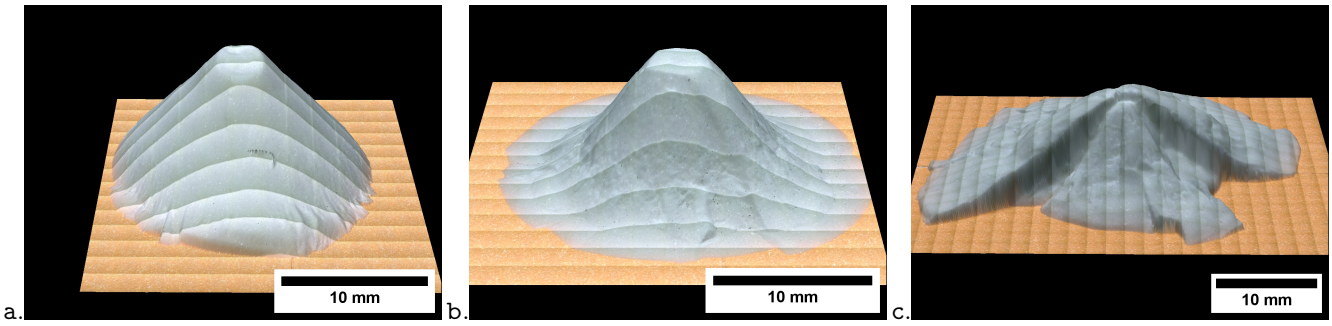

Figure 11: Reconstructions of Sphere Impacted 10mm Al_2O_2 with Cone Formation at 210 m/s (a.), Primary and Secondary Cone Formation at 387 m/s (b.), and Nested Primary and Secondary Cone Formation at 648 m/s (c.).

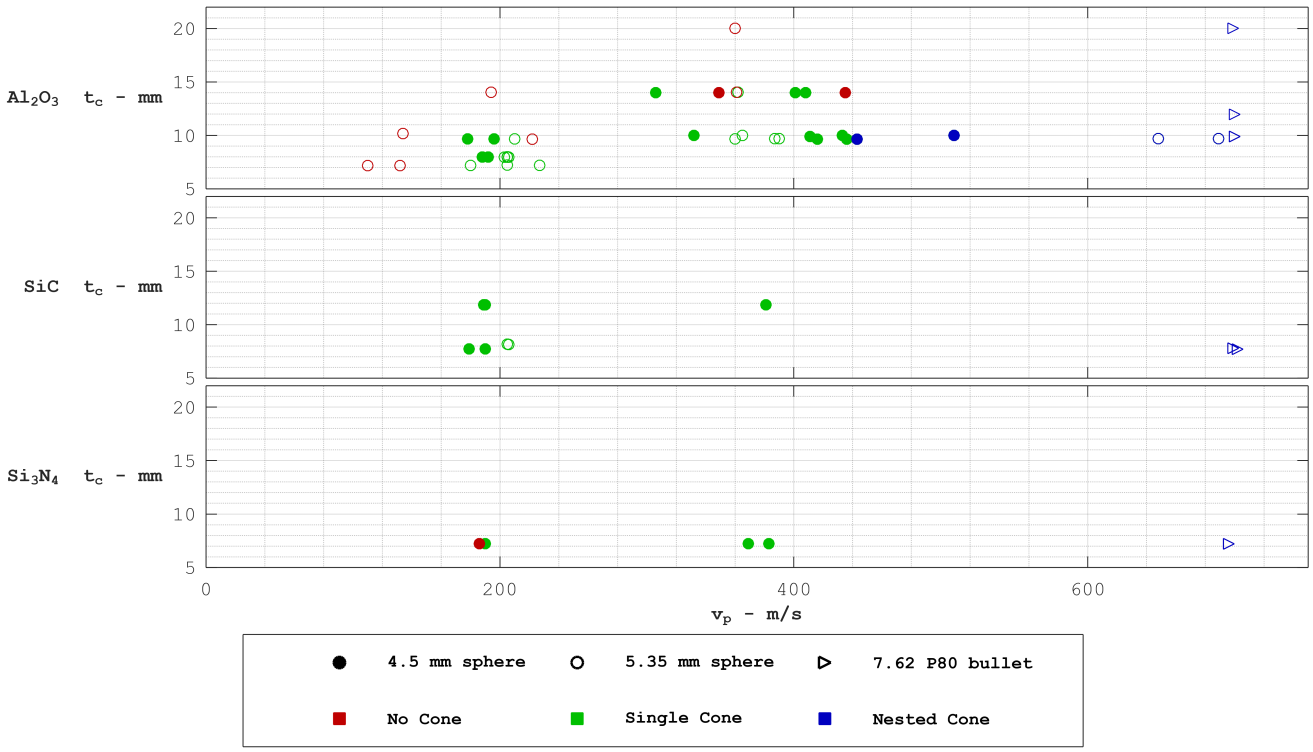

Figure 12: Cone Formation in Ceramic Specimens for Projectile, Impact Velocity, and Tile Thickness.

All sphere impacted specimens were reconstructable, only some tiles were reconstructable for bullet impacts and high speed video recordings were successfully obtained for one Al_2O_2 (10 mm), two SiC (7.8 mm) and one Si_3N_4 (7.2 mm) specimen. Across all ceramic materials, three distinct projectile velocity regimes are identified: a low velocity regime ($v_p \leq 250$ m/s), an intermediate regime (300-550 m/s), and a high velocity regime ($v_p \geq 600$ m/s). The low- and high velocity regimes represent typical low-velocity sphere impact and high velocity bullet impact testing respectively, as expanded on in subsection 1.3.

For alumina impacted in the low- and intermediate velocity regimes, an apparent upper thickness limit is observed beyond which complete cone crack propagation does not occur, identified as a combined geometric and velocity dependent constraint. For sphere impact specimens, the quantity and fineness of cone fragments is observed to increase for greater impact velocity, whereas for bullet impacts the extent of fragmentation is orders of magnitude greater. Nested cones in alumina from sphere impact are only observed at high impact velocities ($\geq$ 443 m/s) for 10 mm tiles. All bullet impacted ceramic tiles formed nested cones and subsequently stepped fracture clouds, characterized by fragment plumes at increasingly spaced radial distances and remnant fragments. Secondary cone angles are observed for all sphere impacted ceramics above intermediate velocities, with one exception (5.35 mm sphere, 206 m/s, 7.96 mm Al_2O_3).

3.2 Macroscopic Cone Geometry

Primary cone angles, secondary cone angles, geometric heights and radii, and nucleation geometry are measured, derived and presented for Al_2O_3 specimens.

3.2.1 Primary Cone Angles as a Function of Impact Velocity

The measured primary cone angles, α_1, together with their 95% confidence intervals (CI), are plotted in Figure 13. Considerable inter-specimen and intra-specimen scatter is observed across the entire velocity range for both single and nested cones. Despite local fluctuations, primary regression analysis indicates no statistically significant dependence of primary cone angle on impact velocity and velocity bins are more evident with stepped shifts over the velocity range.

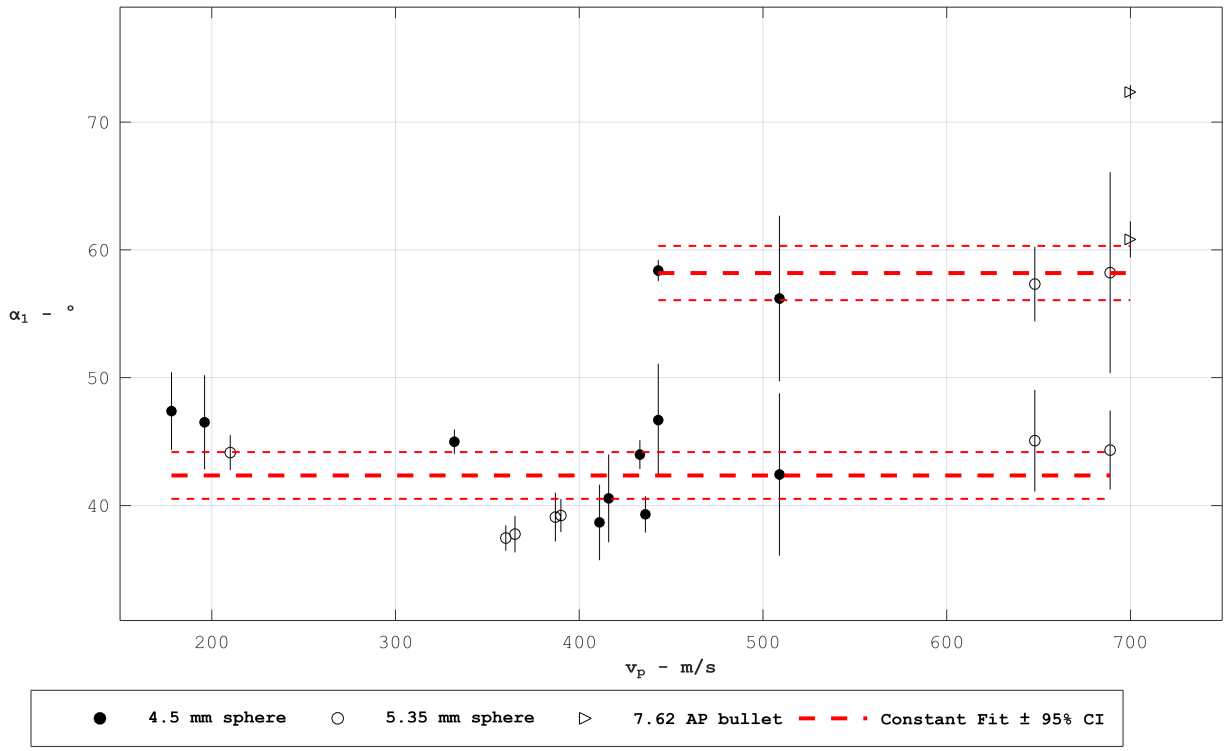

Figure 13: Primary Cone Angles (Mean $\pm$ 95% Confidence Interval) of 10 mm Al_2O_3 with Constant Fits and 95% Confidence Intervals at Single and Nested Cone Angle Regimes.

The sphere impacted specimens display a wide range of mean primary cone angles for the low velocity regime (44-47°), the intermediate regime (37-46°), and the high velocity regime (44-45°) with variation in confidence intervals (±1-6°) over the complete velocity regime. The developed nested cones show greater primary cone angles in the intermediate and high velocity regimes (56-58° and 57-58°) with confidence interval magnitudes similar to single cones (±1-8°). Bullet impacts at 700 m/s produce computed single and nested primary cone angles that exceed the established sphere impacted cone angles with narrow confidence intervals (62±1° and 72±1°). Regression analysis confirmed significance for a second order polynomial ($p = 0.030$), but yields unrealistic values outside the investigated velocity regime (>90°). Within the lower angle regime, a mean primary cone angle of approximately 42° is observed, with residual variations up to 5° and an average mean 95 % confidence interval of ±2°. The nested cone formation is represented by a stable higher angle regime with a mean primary cone angle of approximately 58° and similar confidence level magnitudes (±2°).

To evaluate the presence of additional primary cone cracks, digital microscopy and micro computed-tomography (µCT) are employed for a Al_2O_3 tile impacted at 648 m/s by a 5.35 mm sphere, as visualized in Figure 14.

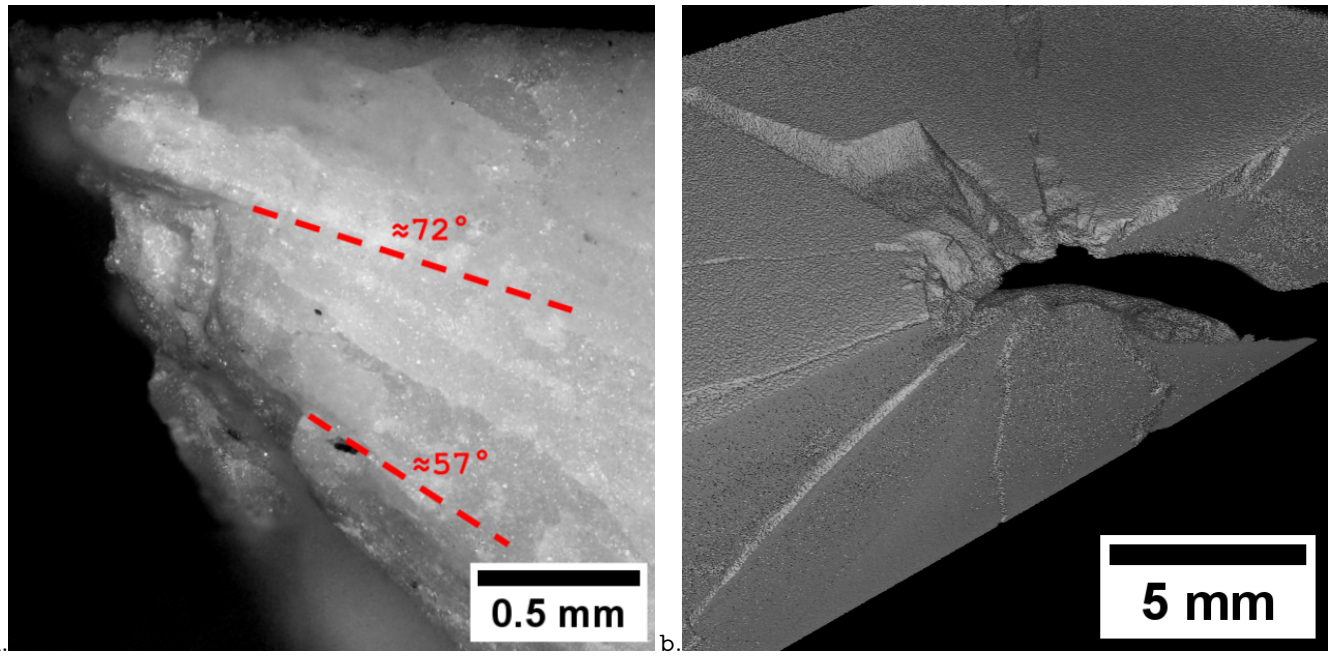

a. b.

Figure 14: Images of Cone Crack Nucleation at 71° Under Digital Microscope (a.) and Absence of a 71° Crack Propagation and in MicroCT Reconstruction (b.).

In the microscope images, found cone angles align with the measured nested cone angles for this specimen (57°) and nucleated cone cone cracks are observed in the higher primary cone angle regime (72°). When investigating internal cracks present in the re-combined tile and cone, no additional propagated cone cracks are observed at this measurement resolution (25µm). Similar propagated and nucleated cone angles (58°, and 71°) are observed in microscopy of the impact site of a Al_2O_3 tile impacted at 689 m/s by a 5.35 mm sphere, however no µCT measurements are conducted for this specimen.

3.2.2 Secondary Cone Angles as a Function of Impact Velocity

The measured secondary cone angles, α_2, together with their 95% confidence intervals, are presented in Figure 15. Secondary cone angles are exclusively observed in the intermediate and high velocity impact regimes. Both inter- and intra-specimen variability exhibit considerable and comparable magnitudes; consequently, no statistically significant trends can be established.

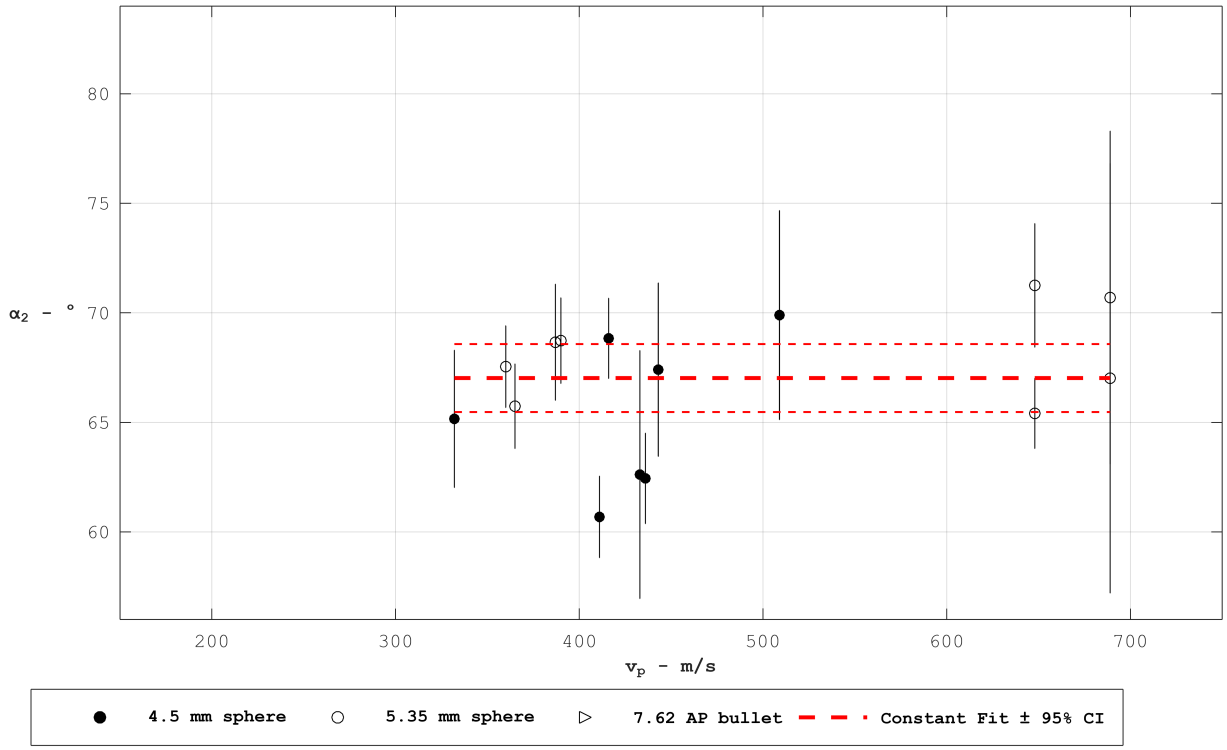

Figure 15: Secondary Cone Angles (Mean $\pm$ 95% Confidence Interval) of 10 mm Al_2O_3 with Constant Fit and 95 % Confidence Interval.

In the intermediate velocity regime, secondary cone angles range between 61-70° with confidence intervals ranging from $\pm$2° to $\pm$6°. Greater inter-specimen variability is observed for the 4.5 mm projectiles compared to the 5.35 mm spheres. At high impact velocities, the 5.35 mm spheres yield cone angles between 65° and 72°, accompanied by wider confidence intervals ($\pm$2-10°) that indicate variability between and within single and nested secondary cone angles. Regression analysis on independent velocity regimes as well as on the combined dataset yields insignificant slope parameters ($p \geq 0.356$) and low coefficients of determination ($R^2 = 0.137$) for first order and second order approximations, with comparable root mean squared error (2.7) as a constant fit (2.9). No statistical foundation for a velocity dependence of secondary cone cracks can be established, and a computed mean secondary cone angle of 67$\pm$2° is interpreted as a rough approximation of the highly scattered response.

3.2.3 Cone Angles as a Function of Tile Thickness and Secondary Cone Height

In Figure 16, primary cone angles are plotted as a function of tile thickness, t_c, while secondary cone angles are related to the maximum measured secondary cone crack height, h_3, as defined in subsubsection 2.3.1. The 10 mm Al_2O_3 cone angles are shown together with thinner and thicker tiles to assess potential inverse linear relationships between cone angles and geometric parameters, as displayed over the data in Figure 16.

7.2 mm and 8 mm tiles impacted by spheres feature slightly greater mean primary cone angles, whereas 14 mm tiles in the intermediate velocity regime exhibit smaller primary cone angles (45–50°, 47–52°, and 32–36° respectively). Bullet impacted 12 mm and 20 mm tiles yield elevated primary cone angles angles (73°$\pm$1° and 58°$\pm$2° respectively). In the lower velocity regime, an inverse first order relationship between primary cone angle and tile thickness is observed, with a slope of approximately -1.0°/mm, however, statistical support for this trend remains weak ($p = 0.103$, $R^2 = 0.224$, CI = $\pm$1.3°). In the intermediate velocity regime, a inverse linear trends is ascertained as the primary cone angle decreases significantly with increasing tile thickness (-2.2°/mm, $p = 0.020$, $R^2 = 0.312$). Higher-order polynomials and an analytical inverse tangent approximations again yield no significant improvement over the linear fit ($p = 0.065$, $R^2 = 0.324$). For bullet impacts, a negative trend between primary cone angle and tile thickness (-0.9°/mm) is observed, but is deficient in statistical support ($p = 0.424$, $R^2 = 0.332$, CI = $\pm$3.9°, $n = 4$).

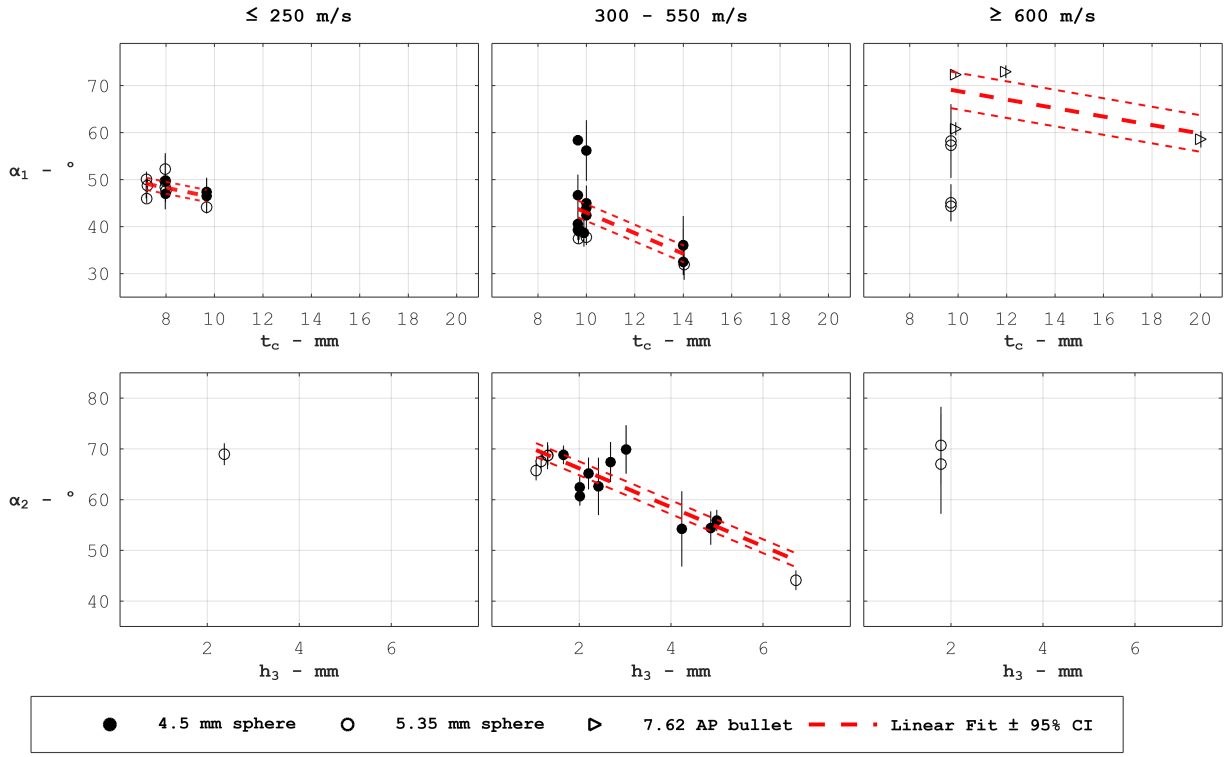

Figure 16: Primary and Secondary Cone Angles (Mean ± 95% Confidence Interval) over Tile Thickness and Formation Height of Al_2O_3 with Linear Fits and 95% Confidence Intervals.

For 14 mm tiles, secondary cone angles are lower compared to the 10 mm specimens (54–56° ±2–7° and 44±2° respectively). Additionally, secondary cone cracks in 14 mm tiles initiate at greater distances from the rear surface (4.2–5.0 mm and 6.7 mm) compared to 10 mm tiles (1.7–3.0 mm and 1.0–1.3 mm). A statistically supported inverse linear trend is found as the secondary cone angle decreases with increasing secondary cone height (-3.8°/mm, $p \leq 0.001$, $R^2 = 0.706$). Higher-order polynomials and an analytical inverse tangent approximations yield a negligibly more significant ($p \leq 0.001$, $R^2 = 0.785$), where the linear fit is accepted for relative simplicity.

3.2.4 Cone Nucleation Geometry as a Function of Projectile Geometry and Velocity

The combined cone formation depth, h_c, computed as the initial tile thickness minus the measured cone top height h_1, together with the truncated cone radius r_1, provides insight into cone crack nucleation geometry in Al_2O_3. The relationship between h_c and r_1 for different velocity regimes and projectile geometries is visualized in Figure 17. Across all tile thicknesses, smaller 4.5 mm sphere projectiles consistently produce smaller truncated cone radii and lower cone nucleation depths relative to the 5.35 mm spheres, with limited influence of impact velocity.

In the low velocity regime ($\leq$ 250 m/s), 4.5 mm spheres impacted tiles yield low mean truncated radii (0.62–0.72 mm) and analogous low nucleation distances (0.30–0.90 mm), whereas the 5.35 mm sphere impacted specimens exhibit larger radii (1.06–2.03 mm) and greater nucleation depths (0.93–3.22 mm). Within the intermediate velocity regime (300–550 m/s), a similar distinction in geometric response between spherical projectile sizes is maintained (r_1 = 0.20-0.71 mm, h_c = 0.15-1.40 mm for 4.5 mm and r_1 = 1.50-2.21 mm and h_c = 1.43-2.11 mm for 5.35 mm sphere). Singular outliers are observed for small and large spheres (1.43/2.32 mm and 0.50/0.46 mm) but are regarded as anomalies and excluded from geometric distinction between spherical projectile types. Cone specimens created by 5.35 mm spheres at impact velocities greater than 600 m/s are scarce (n=2), but show radii and nucleation depths consistent with previously established ranges (1.42–1.46 mm and 1.39–2.17 mm respectively).

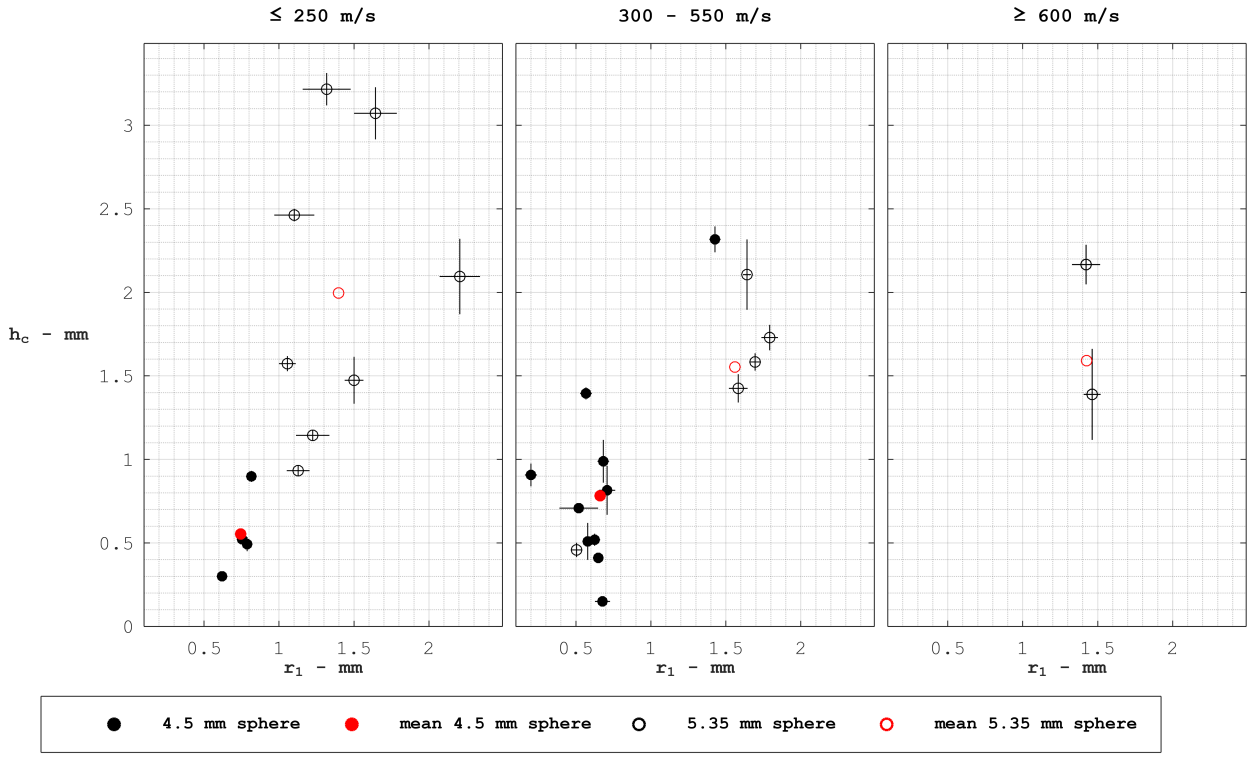

Figure 17: Cone Crack Nucleation Depth (Mean ± 95% Confidence Interval) over Nucleation Radius (Mean ± 95% Confidence Interval) of Al_2O_3 with Mean Projectile Values per Velocity Regime.

For the 4.5 mm spheres, the mean truncated radius remains relatively stable between the low and intermediate velocity regimes (0.744 mm to 0.661 mm), whereas the mean nucleation depth increases marginally (0.554 mm to 0.782 mm). For the 5.35 mm spheres, mean truncated radii show slight variation across velocity regimes (1.397 mm, 1.560 mm, and 1.426 mm), accompanied by a slight reduction in mean nucleation depth (1.997 mm, 1.553 mm, and 1.591 mm). A slight convergence of mean nucleation depth is attributed to isolated outliers and is statistically inconclusive from the absence of high velocity 4.5 mm sphere impacted specimens.

3.3 Surface Roughness Evolution along the Cone Crack Path

The arithmetic surface roughness, R_a, at five incremental measurement lines is evaluated for different tile thicknesses, projectile types, and velocity regimes. Both raw and normalized roughness values are analysed to assess the evolution of fracture surface morphology along the cone flank. Normalized roughness values are scaled relative to $R_{a,1}$ to minimize axial misalignment and highlight relative progressions. The normalized arithmetic surface roughness values, mean values and corresponding 95% confidence intervals are visualized in Figure 18.

For sphere impacts at low velocity, raw roughness values remain comparatively moderate. Smaller 4.5 mm spheres generally exhibit lower absolute roughness values (45-546 µm) compared to 5.35 mm spheres (61-962 µm). However, the normalized data reveals an average consistent roughness increase from the top to the lower cone region for 4.5 and 5.35 mm projectiles (x2.3 and x1.5 respectively). The thinnest 7.2 mm tiles show the lowest absolute roughness values (75-264 µm), with 8 mm tiles showing the greatest roughness values (78 - 963 µm), and 10 mm tiles show intermediate values (45-546 µm), which reflect in the mean raw roughness values (127, 228, and 212 µm respectively). The normalized data indicates homogeneous progressive roughness amplification over the cone flank for all thicknesses (x1.4, x1.6, and x2.4). At velocities ranging from 300-500 m/s, the roughness magnitude increases substantially for both projectile diameters. Smaller spheres yield greater roughness values (61-570 µm) compared to 5.35 mm spheres (41-342 µm) and the normalized data indicates a progressively weakening average roughness increase from top to bottom for both projectiles (x1.9 and x1.4 average). For 10 mm and 14 mm tiles similar raw and normalized roughness values were observed (61-511 µm and 42-570 µm) with aligning progressively weakening average roughness increases (x1.7 and x1.8 average). At high impact velocities, roughness evolution shows greater variability between projectiles and less relative growth. For

5.35 mm spheres, raw surface roughness magnitudes are comparable to those found in the intermediate regime (101-464 µm) and show significant initial growth in normalized surface roughness, but gradually decrease when at greater distances from the cone top to yield a moderate average increase (x1.4). Whereas bullet impacted tiles produce the largest absolute roughness magnitudes (534-1505 µm), with a variable progressive roughness amplification (x1.8) over the cone fracture surface.

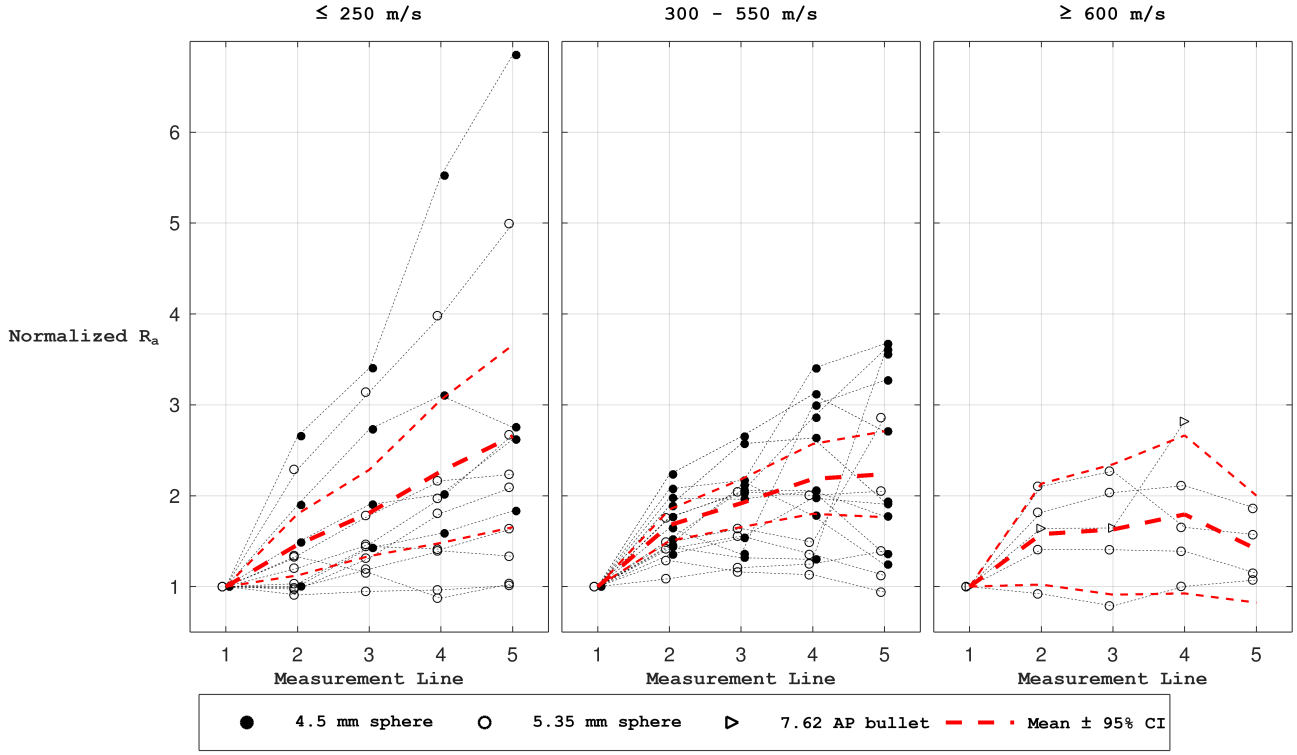

Figure 18: Normalized Arithmetic Surface Roughness over Line Measurement Locations with Mean Values and 95% Confidence Intervals per Measurement Line.

The normalized roughness data allows significant identification of global trends, but shows excessive variability for regression fitting for first ($\leq$250 m/s: $p \leq 0.001$ $R^2 = 0.255$, 300-550 m/s: $p \leq 0.001$ $R^2 = 0.372$, $\geq$600 m/s: $p \leq 0.134$ $R^2 = 0.099$) and second order polynomials ($\leq$250 m/s: $p \leq 0.001$ $R^2 = 0.255$, 300-550 m/s: $p \leq 0.001$ $R^2 = 0.372$, $\geq$600 m/s: $p = 0.037$ $R^2 = 0.269$). In the low and intermediate velocity region the mean magnification factor is the greater than for the high velocity regime (x1.2, x1.25 and x1.12). These trends are visually observable in the different mean normalized R_a per measurement location from Figure 18, where a constant linear trend is observed for low impact velocity specimens, a rapidly amplified but stagnating mean is observed for the intermediate velocity regime, and an amplified initial and highly stagnated mean is found for the high velocity regime.

3.4 Microscopic Cone Fracture Surface

The cone crack fracture surfaces of Al_2O_3 specimens are examined at incremental locations using SEM at multiple magnification levels to identify fracture features at various length scales. Minor variations are observed along the side cone fracture surfaces profiles, with no consistent trends, however near the comminuted zone distinctive microstructural features are identified untypical for brittle ceramic fracture fracture morphology.

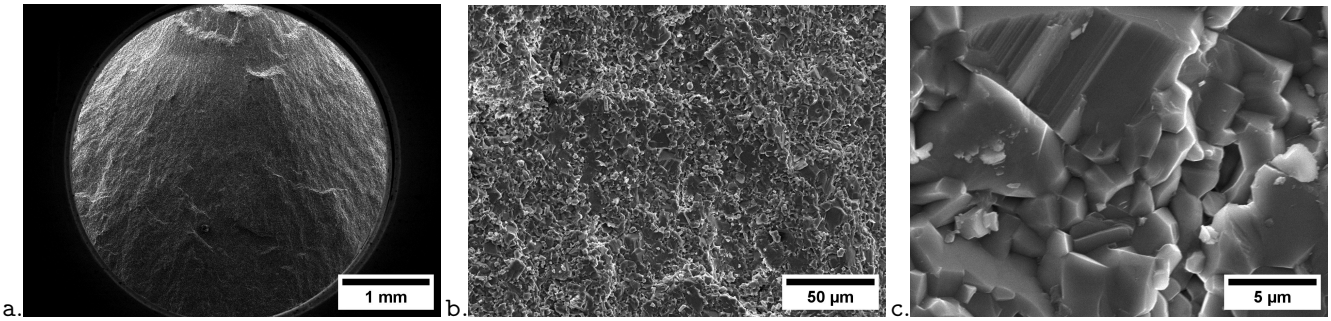

Figure 19: SEM Images of Cone Fracture Surface of Sphere Impacted Al_2O_3 at 25x (a.) 500x (b.) and 5000x (c.) magnification.

The fracture surfaces display characteristic brittle fracture behaviour, as shown in Figure 19. At low magnification (25x) morphology and surface irregularities are observable. At intermediate magnifications (100x-500x), ridges, microcracks and granular features are visible. At 1000x magnification fracture surfaces with grain boundaries and transgranular facets are are distinguishable. High magnification imaging (5000x) allows identification of triple junction pores, cleavage marks (striations, hackles and micro-steps), micro-pores, dimples and micro-particulates. Quantification is performed at 1000x magnification to balance surface area and feature resolution, with verification at 5000x magnification. Both intergranular (IG) and transgranular (TG) fracture modes are identified for all projectiles types and velocity regimes, as shown in Figure 20.

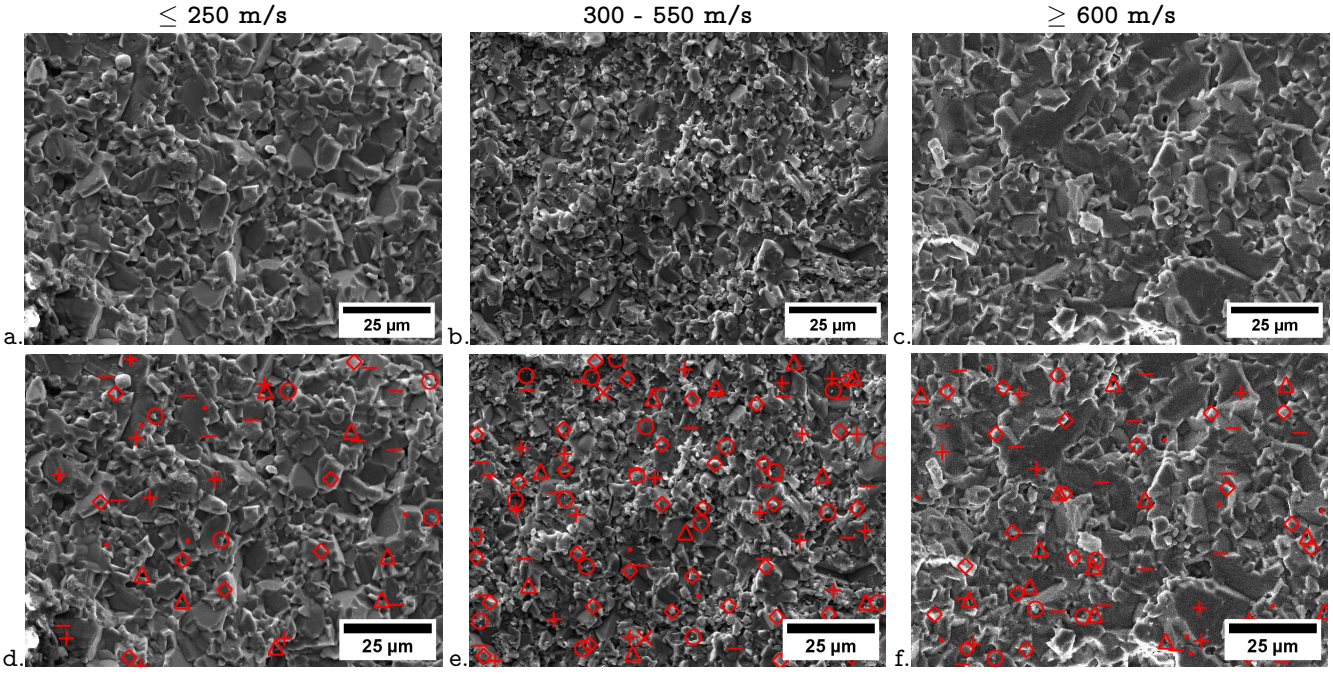

Figure 20: SEM Images of Cone Fracture Surface of Sphere Impacted Al_2O_3 at 1000x magnification (a.-c.) and Damage Identifications (d.-f.). ($\diamond$: grain boundary, $\triangle$: triple junction pore, $-$: flat fracture plane, $+$: cleavage, $\cdot$: micro-pores / dimples, X: secondary crack, O: micro-particulates)

Sphere impacted specimens show comparable exposed grain boundaries for low, intermediate, and high velocity regimes (47, 52, 41 % respectively), similar to bullet impacts (50 %). Triple junction pore densities are moderate for all regimes and lower density for increased velocity ranges (36, 38, and 28 % respectively), with a slight reduction for bullets (22 %). Smooth transgranular fracture surfaces are consistently identified for all sphere impact velocity regimes (63, 67, and 68 %) and slightly increase for bullet impacts (75 %). Cleavage marked transgranular fracture features occur at lower relative frequencies for spheres (40, 39, 29 %) and bullets (42 %). Secondary damage modes are identified in trace to low extents (0-32 %) for the all velocity regimes; dimples are rare in all specimens ($\leq$ 12), secondary cracks are negligible ($\geq$1 %), and secondary particles are consistently present (17%-32%).

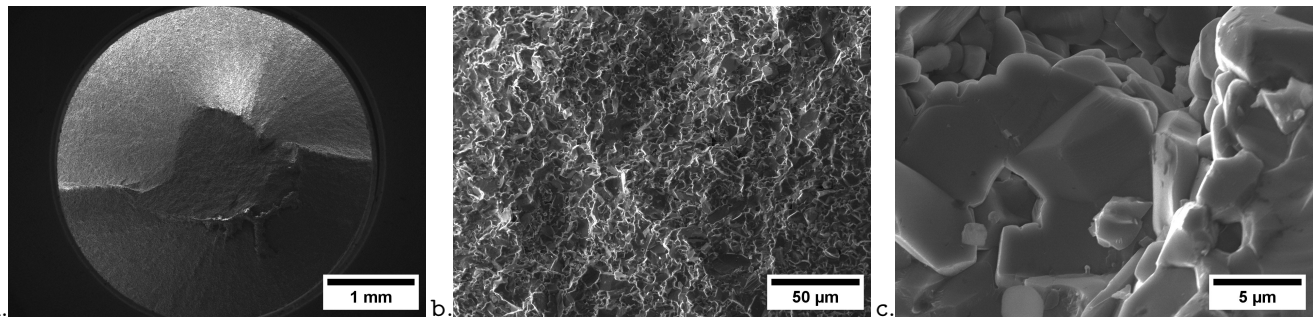

Figure 21: SEM Images of Al_2O_3 Cone Top Fracture Surface at 25x (a.), 500x (b.), and 5000x (c.) magnification.

Although mixed brittle fracture features are observed near the comminuted zone for all sphere impacted specimens, as shown in Figure 21, non-typical smooth and rippled microstructure are observed for increased velocities ($\geq$ 400 m/s). Cone tops reveal higher relative areal densities of exposed grain boundaries (47-95 %) and triple junction pores (42-85 %). Furthermore, significant scatter of flat transgranular fracture features and cleavage features are observed (13-83 % and 2-56 %) and are less pronounced in the intermediate regime. Dimples are scarcely observed ($\leq$ 11 %), secondary cracks appear sporadically ($\leq$ 7 %), and secondary particle identification densities are moderate (39-52 %). At velocities above approximately 400 m/s local smooth fracture and repetitive ripples are observed near the cone top for both sphere and bullet impacts, as shown in Figure 22, with EDS measurements identifying purely Al_2O_3, and a hypothesis discussed in section 4.

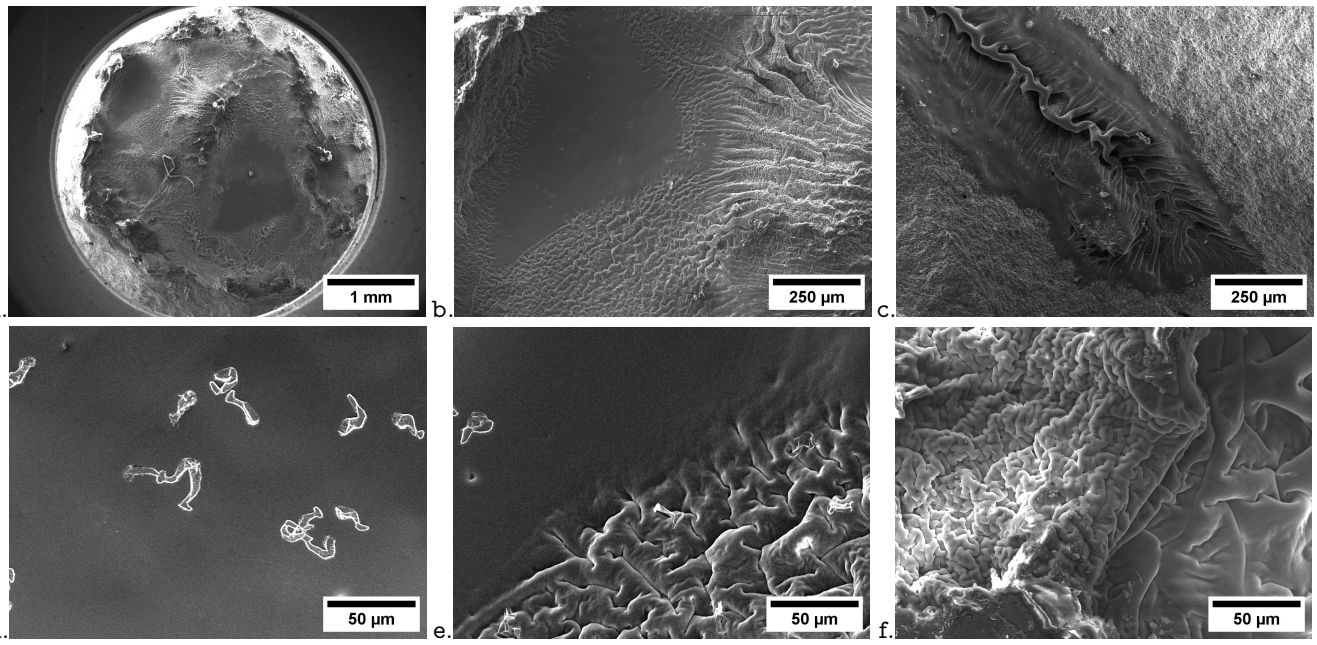

Figure 22: SEM Images of Top Fracture Surfaces with Smooth and Rippled Microstructure of Impacted ($\geq$ 400 m/s) Al_2O_3 at 25x (a.), 100x (b.-c.), and 500x (d.-f.) magnification.

The percentage of intergranular fracture, $\%_{IG}$, is computed from the exposed grain boundaries density, ρ_{GB}, triple junction density, ρ_{TJ}, flat fracture surfaces density, ρ_{FF}, and cleavaged marked density, ρ_{CM}, according to Equation 11.

$$\%_{IG} = \frac{\rho_{IG}}{\rho_{IG} + \rho_{TG}} = \frac{\rho_{GB} + \rho_{TJ}}{\rho_{GB} + \rho_{TJ} + \rho_{FF} + \rho_{CM}} \tag{11}$$

For all velocity regimes, the cone fracture surfaces show mixed intergranular and transgranular fracture modes, as visualized in Figure 23, in accordance with found relative areal density values. As cone top fracture is influenced by local impact conditions rather than cone crack fracture mechanics, and is not retrieved for bullet impacted specimens, quantitative fracture mode analysis excludes top top surfaces for consistency.

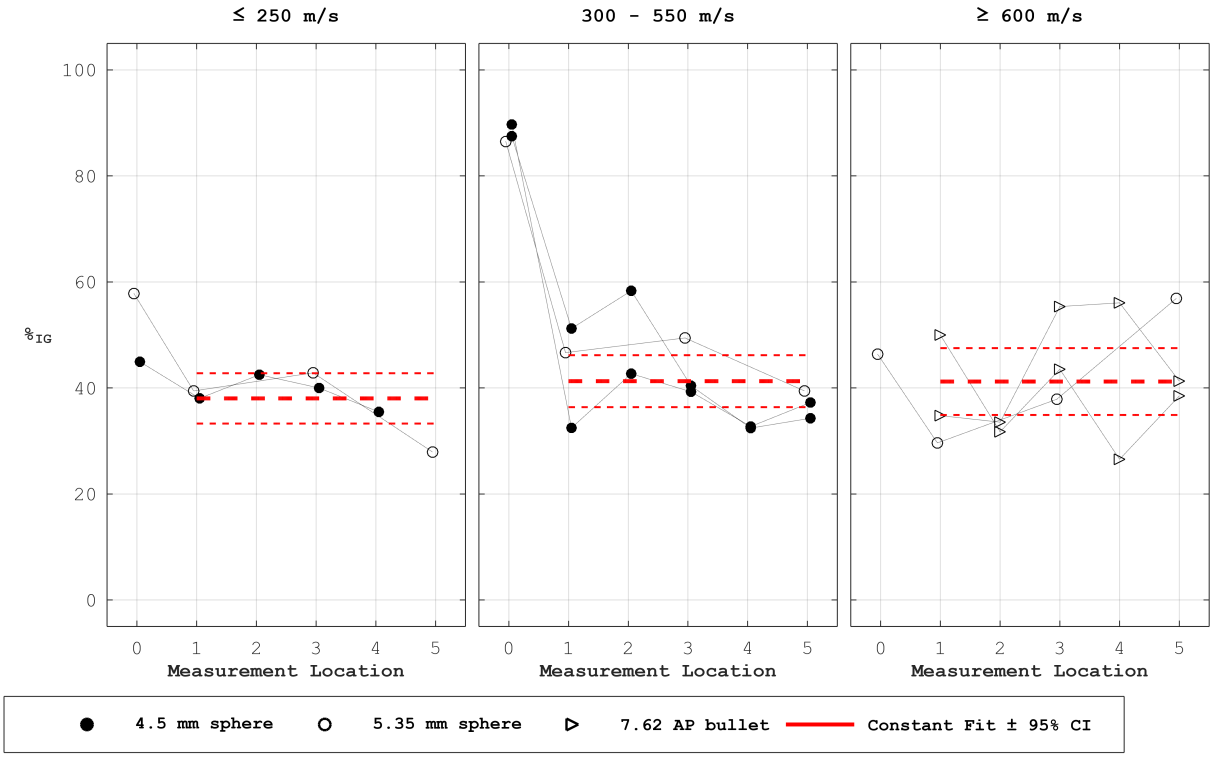

Figure 23: Computed Percentage of Intergranular Fracture, from Equation 11, at Incremental Measurement Locations for Velocity Regimes and Projectiles with Mean Constant Fit and 95% Confidence Intervals.

At lower, intermediate, and high velocity regimes moderate intergranular fracture percentages are found (27-43 %, 32-58 %, and 25-57 % respectively), with comparable moderate ranges for bullet impacts (26-56 $). Constant mean intergranular fracture percentage fits are consistent over the velocity regimes (38 %, 41 %, and 41 %), with narrow confidence intervals ($\pm$5 %, $\pm$5 %, and $\pm$6 %). A significant second order polynomial with strong predictive capability is identified for the lower velocity regime ($p = 0.001$, $R^2 = 0.960$), however the measurement quantity at this measurement location is low (n=1). From the other regimes no statistical significant dependence of the percentage of intergranular fracture on projectile geometry, impact velocity, or tile thickness is identified ($p \geq 0.05$), variations are within measurement uncertainty, and top-surface effects are regarded as near-impact transition effects.

3.5 Extension to SiC and Si_3N_4

Experimental and characterization investigations into SiC and Si_3N_4 are conducted at macroscopic, mesoscopic and microscopic scales to identify similarities and differences in cone crack features assignable to material properties.

3.5.1 Primary and Secondary Cone Angles over Projectile Velocity

Primary and secondary cone angles are plotted as a function of projectile velocity in Figure 24. Sphere impacted specimens display low inter-specimen variation within individual velocity regimes. Bullet impacts exhibit distinct elevated nested cone angles relative to sphere impacts. Statistical foundation for trends is limited for both materials.

For sphere impacted 7.9 mm SiC ceramic tiles, similar cone angles are measured for 4.5 mm spheres and 5.35 mm spheres in the low velocity regime (38-46° and 39-42° respectively), whereas bullet impacts result in significantly greater primary cone angle regimes (52-57° and 70-77°). Sphere impacted Si_3N_4 tiles show a reduction in primary cone angles from the low velocity regime (48°) to the intermediate velocity regime (33-34°), whereas bullet impacts produce three measured primary cone angles (36°, 65°, and 76°). Secondary cone angles are only observed for Si_3N_4 in the intermediate velocity regime (67-71°).

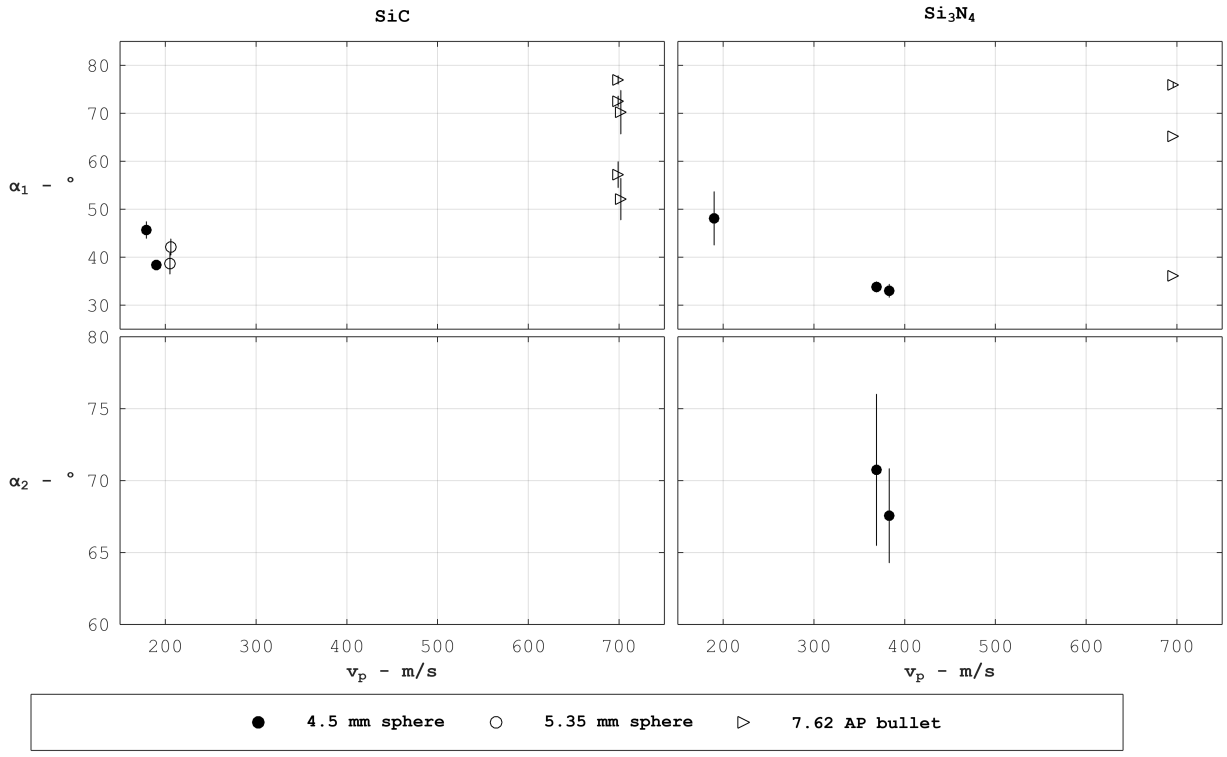

Figure 24: Primary and Secondary Cone Angles (Mean $\pm$ 95% Confidence Interval) over Projectile Velocity for 8 mm SiC and 7.2 mm Si_3N_4 Specimens.

Due to limited specimen numbers, regression analysis lacks statistical foundation ($n \leq 4$), however a descriptive negative trend for the primary cone angle with increasing velocity is observed for Si_3N_4, converging to the minimal bullet cone angle. Maximum primary cone angles generated by bullet impacts are of comparable magnitude for SiC and Si_3N_4, but are no valid metric as tile thicknesses differ.

3.5.2 Primary and Secondary Cone Angles over Geometric Thickness and Height

The primary and secondary cone angles of sphere impacted Al_2O_3, SiC, and Si_3N_4 specimens up to 400 m/s are plotted in Figure 25. Consistent with the trends reported in subsubsection 3.2.3, negative linear relationships are identified between primary cone angles and tile thickness, and between secondary cone angle and secondary cone crack formation height for Al_2O_3 and SiC. Data availability of Si_3N_4 is limited.

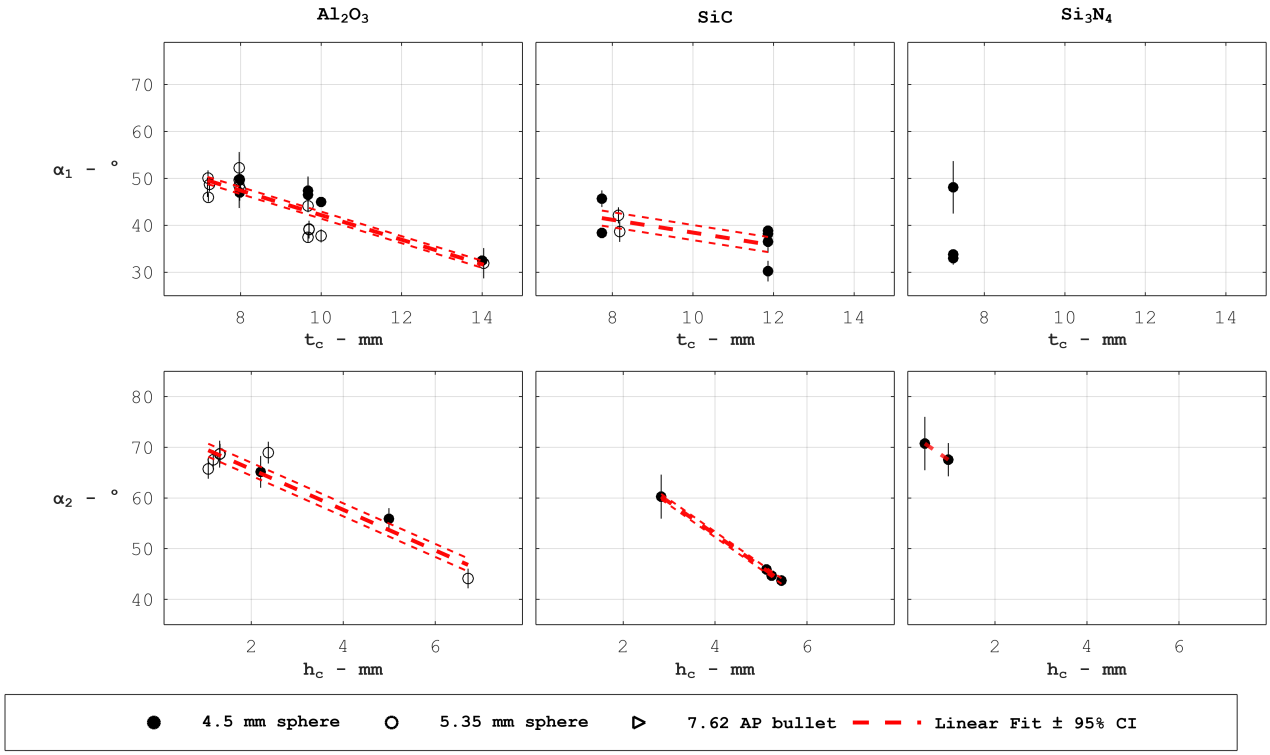

Figure 25: Primary and Secondary Cone Angles (Mean ± 95% Confidence Interval) over Tile Thickness and Formation Height of Ceramic Materials with Linear Fits and 95% Confidence Intervals.

The magnitude of primary and secondary cone angles for SiC and Si_3N_4 (30-48° and 44-77°), as well as secondary cone crack formation heights (0.5-5.4 mm) are comparable to those measured for Al_2O_3 specimens (32-52°, 44-77°, and 1.1-6.7 mm), indicating similar geometric fracture scales despite dissimilar mechanical properties.
The primary Al_2O_3 cone angle reveals a strong negative linear dependence on tile thickness (-2.6°/mm), with substantially significant statistical foundation and predictive capability ($p \leq 0.001$, $R^2 = 0.750$, CI = 0.7°). The SiC primary cone angles show a comparable but weaker negative slope (-1.4°/mm), with reduced statistical support ($p = 0.083$, $R^2 = 0.418$, CI = 1.6°).

For secondary cone angles, all three ceramics demonstrate a negative relationship with secondary cone formation height (-4.0 °/mm for Al_2O_3, -6.4 °/mm for SiC, and -6.2 °/mm for Si_3N_4). Robust statistical support is obtained for Al_2O_3 and SiC (Al_2O_3: $p \leq 0.001$, $R^2 = 0.906$, CI = ±1.29°; SiC: $p \leq 0.001$, $R^2 = 0.992$, CI = ±0.54°), whereas the limited quantity of Si_3N_4 specimens inhibits statistically meaningful regression analysis (n=2).

3.5.3 Cone Nucleation Depth and Truncated Radius Scaling

The computed cone nucleation depth and minor truncated cone radius of sphere impacted Al_2O_3, SiC, and Si_3N_4 specimens up to 400 m/s are plotted in Figure 26. Consistent geometric distinctions between projectile sizes are identified for Al_2O_3 and SiC, with marginal differences in cone nucleation geometry for all investigated ceramics.

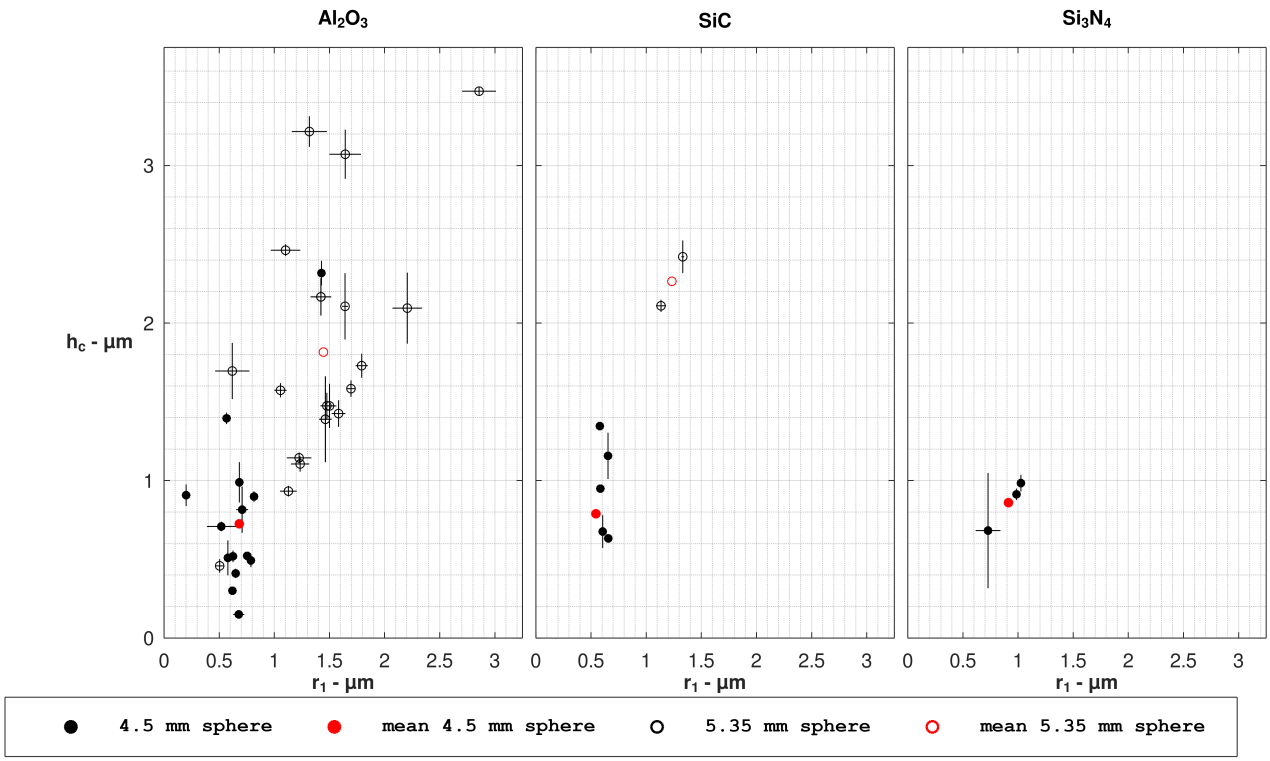

Figure 26: Cone Crack Nucleation Depth (Mean ± 95% Confidence Interval) over Nucleation Radius (Mean ± 95% Confidence Interval) with Mean Projectile Values per Ceramic Material.

For Al_2O_3, significant differences in mean nucleation depth and truncated cone radius are observed between smaller projectiles (0.68/0.72 mm) and larger projectiles (1.45/1.82 mm), as presented in subsubsection 3.2.4. Comparably, SiC specimens impacted by smaller and larger projectiles exhibit similar scaling behaviour (0.54/.0.79 mm, 1.26/2.27 mm), and Si_3N_4 specimens show moderately greater mean nucleation depths and radii (0.91 mm and 0.86 mm) for small projectiles, but are limited in sample size (n=3).

3.5.4 Surface Roughness Evolution over Crack Propagation

The arithmetic surface roughness, R_a, measurement at incremental cone heights is analysed SiC and Si_3N_4 within the previously defined projectile impact velocity regimes. Both raw and normalized values are evaluated to identify mesostructural evolution over the crack propagation for different intrinsic material properties. The normalized R_a values, together with mean values and corresponding 95% confidence intervals, are visualized in Figure 18.

For thin SiC tiles, comparable raw roughness magnitudes are measured for small and large projectiles at low impact velocities (86-242 µm and 86-219 µm respectively). For thicker SiC tiles, greater roughness values at both low and intermediate velocity regimes are quantified (57-493 µm). Normalized roughness values for thin SiC tiles reveal moderate amplification (x1.1 - x2.0), whereas thicker tile show larger incremental amplifications (x1.8-x2.4), indicating general progressive roughness development despite local variability.

In contrast, Si_3N_4 cones exhibit greater raw roughness values at low impact velocities (102-402 µm) compared to intermediate impact velocities (86-192 µm) for 4.5 mm projectiles. Correspondingly, the mean normalized amplification factor is greater in the low velocities regime than in the intermediate velocity regime (x2.4 and x1.4-1.5 respectively), although both indicate consistent progressive roughness amplification from the top to the lower cone region. Below 250 m/s a statistical significant fit is found for a linear ($p \leq 0.001$) and a second order polynomial ($p \leq 0.001$) correlation between surface roughness and crack propagation length, but the degree of variability is unexplained by the either fit ($R^2 \leq 0.618$). For Si_3N_4 regression analysis is statistically inappropriate as sample size in low ($n \leq 2$)

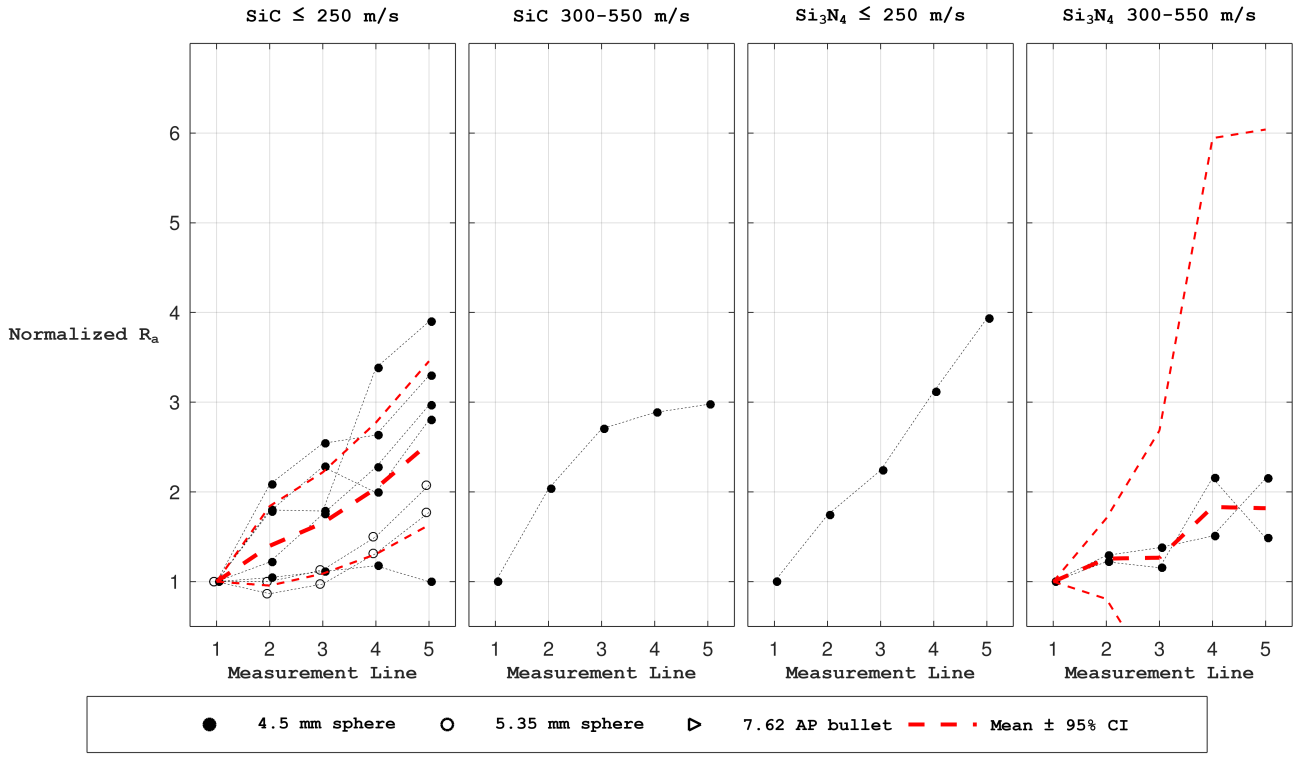

Figure 27: Normalized Arithmetic Surface Roughness over Line Measurement Locations with Mean Values and 95% Confidence Intervals per Measurement Line for SiC and Si_3N_4.

3.5.5 Fracture Mode Identifications and Ratios in SiC and Si_3N_4.

Top and side cone fracture surfaces of SiC and Si_3N_4 specimens impacted at low impact velocities ($\leq$ 250 m/s) by 4.5 mm spherical projectiles are investigated similarly to subsection 3.4.

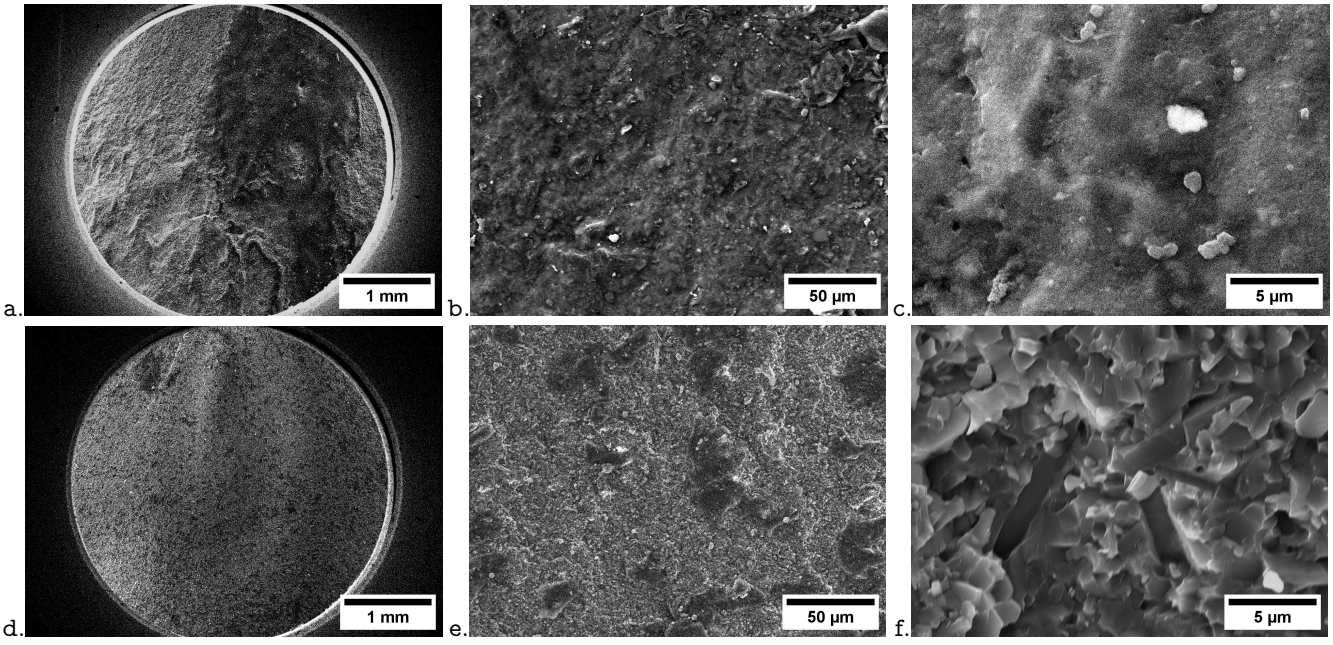

Figure 28: SEM Images of Cone Fracture Surface of Sphere Impacted SiC (a.-c.) and Si_3N_4 at (d.-f.) 25x, 500x, and 5000x magnification.

Representative SEM images of SiC and Si_3N_4 cone fracture surfaces are shown in Figure 28, with characteristic distinguishable brittle fracture modes. For SiC cones, mesoscopic fracture planes and imperfections are visible at 25x magnification, predominantly smooth facets with clustered exposed grain boundaries are observed at 500x magnification, and micro-particulates, voids, and geometric granular remnants are distinguishable at 5000x magnification.

Alternatively, SEM images of Si_3N_4 cones reveal a smooth fracture surface with dispersed colour contrast at 25x magnification, clustered glassy features within a distinctly granular bulk at 500x magnification, and sharp exposed grained boundaries, translucent regions, and a lack of distinguishable secondary damage modes at 5000x magnification.

The analysed SiC cone side fracture surfaces show exposed characteristic grain boundaries and triple junction pores at relatively low areal densities (14 % and 5 % respectively), whereas greater occurrence densities are observed for flat transgranular fracture surfaces and transgranular cleavage marks (96 % and 25 % respectively). Secondary fracture features such as granular dimples, secondary cracks and micro-particulates are identified in relatively less occurrences (7 %, $\leq$1 %, and 26 %).

Inversely, in Si_3N_4 cone fracture surfaces very high areal densities of exposed grain boundaries are distinguished (93 %), whereas significantly less flat transgranular fracture surfaces are observed (31 %). The finer ceramic grains impede confident distinguishment of intergranular triple junction pores, transgranular cleavage marks, dimples, and micro-particulates, which are consequently excluded from evaluation of fracture mode percentages.

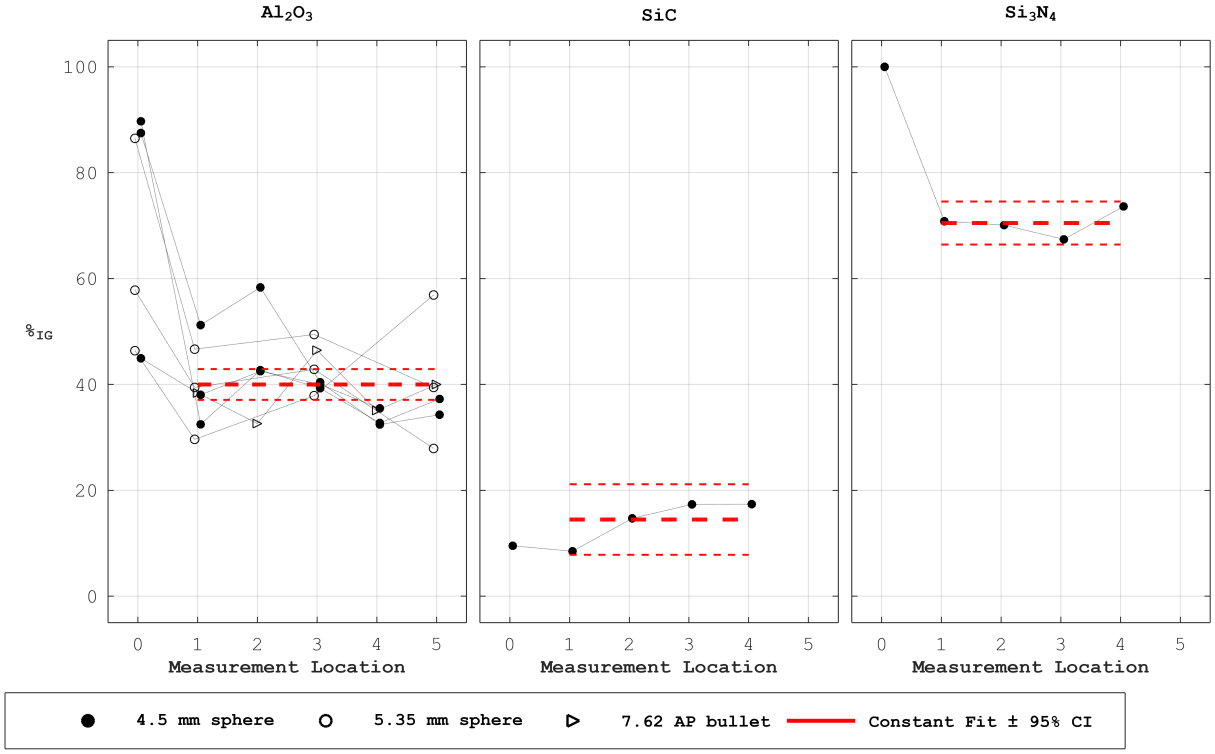

Figure 29: Computed Percentage of Intergranular Fracture, from Equation 11, at Incremental Measurement Locations for Ceramic Materials and Projectiles with Mean Constant Fit and 95% Confidence Intervals.

The calculated intergranular fracture percentage, $\%_{IG}$, and the mean constant fits, are plotted in Figure 29. For SiC consistently low intergranular fracture percentages are calculated along the crack propagation surface (8-17 %), reflected in a low mean constant fit and narrow 95% confidence interval (14$\pm$7 %). For Si_3N_4, high intergranular fracture percentages are computed (67-74 %), with an extreme value at the cone top (100 %), yielding a high mean percentage intergranular fracture and narrow confidence interval over the side cone fracture surface (70$\pm$4 %). Regression fitting is considered statistically invalid for the low quantity of SiC and Si_3N_4 specimens.

3.6 Summary of Results

The derived correlations and support are listed in Table 12 and Appendix 3 for macroscopic cone geometry, mesoscopic topology, and microscopic fracture modes related to cone crack formation.

Table 12: Summary of Results for Cone Crack Geometry, Surface Topology, and Fracture Modes.

Projectile[1]	Ceramic	Correlation	v_p - m/s	t_c - mm	Support
● ❍	Al_2O_3	$\alpha_1 \approx \begin{cases} 42° \\ 58° \\ 72° \end{cases}$	175–700	10	No significant trend, narrow CI (±5%)
			≥600	10	Microscopy measurements (n=2)
▬►	Al_2O_3	$\alpha_1 \approx \begin{cases} 62° \\ 72° \end{cases}$	700	10	High speed video measurements (n=1)
● ❍	Al_2O_3	$\alpha_1 \propto -t_c$	300–550	7.2–14	p = 0.020, R^2 = 0.312
●	SiC		≤400	8	p = 0.083, R^2 = 0.418
● ❍	Al_2O_3	$\alpha_2 \propto -h_3$	300–550	-	p ≤ 0.001, R^2 = 0.706
●	SiC		≤400	-	p ≤ 0.001, R^2 = 0.992
● ❍	Al_2O_3 SiC	$h_c \propto r_p$	175–700 ≤400	7.2–14 7.8–12	Consistent geometric scaling
● ❍	Al_2O_3 SiC	$r_1 \propto r_p$	175–700 ≤400	7.2–14 7.8–12	Consistent geometric scaling
● ❍	Al_2O_3	$R_a \propto$ crack propagation	175–700	7.2–14	p ≤ 0.001 R^2 ≤ 0.372
	SiC		≤250	8	p ≤ 0.001, R^2 = 0.618
●	Si_3N_4		≤550	7.2	Descriptive trends (n≤2)
● ❍	Al_2O_3	$\%_{IG} \approx 41\%$	175–700	7–14	No significant trend, narrow CI (±5%)
●	SiC	$\%_{IG} \approx 14\%$	≤250	8	Mean 14±7% (n=1)
●	Si_3N_4	$\%_{IG} \approx 70\%$	≤250	7.2	Mean 70±4% (n=1)

[1]: ● 4.5 mm sphere, ❍ 5.35 mm sphere, ▬► 7.62 P80 bullet.

For sphere impacts on 10 mm Al_2O_3 tiles, the primary cone angle, α_1, is found to show discrete plateaus, rather than a continuous trends for impact velocity. A transition to nested cones is observed around 400 m/s, and above 600 m/s a larger nucleation angle is identified from secondary measurements in limited quantities. For bullet impact larger primary cone angles are distinguished, similar in magnitude to sphere impacted nested cones.

Statistically significant inverse linear relationships for Al_2O_3 and SiC between primary cone angle and tile thickness, t_c, are found for first and second order polynomials. Similarly, secondary cone angle, α_2, and the secondary cone angle formation height, h_3, are exhibit strong statistical correlations and explanatory power of variability between specimens.

The cone nucleation depth, h_c, is derived from the distance between tile thickness and top cone height, $h_1 a$, and is found to be independent of ceramic material and impact velocity. Similarly, the minor cone radius, r_1, is found to be independent of material and sphere velocity. Both nucleation depth and minor radius scale proportionally for Al_2O_3 and SiC, with limited data on Si_3N_4.

The normalized surface roughness, R_a, is computed and is found to increase progressively along the crack propagation path, independently of projectile type and ceramic material, and with minor shifts for impact velocity. The trends match statistically significant first and second order polynomials, but with limited explanatory power of inter-specimen variability.

The percentage of intergranular fracture, $\%_{IG}$, is calculated from relative occurrences of characteristic fracture marks. No statistical trend is observed for $\%_{IG}$ as a function of velocity or projectile type for Al_2O_3, and discrete fracture modes are identified for different ceramic materials.

Independently, these results demonstrate strong statistical support for established (a_1/t_c) and exploratory correlations (a_2/h_3), display geometric scaling and topological trends (h_c/r_1, R_a), while expected geometric and material correlations (a_1/v_p and $\%_{IG}/K_{IC}$) are not observed in the investigated regimes.

4 Discussion

The correlations found in this investigation indicate that cone crack morphology in ceramics is governed predominantly by geometric conditions, while intrinsic material properties primarily influence fracture modes at the microscale. Across Al_2O_3, SiC and Si_3N_4, consistent scaling relationships are identified that distinguish nucleation-controlled phenomena from propagation-controlled behaviour. The research questions are answered with the available information and uncertainties and statistical insufficiencies are highlighted.

RQ1 — How do impact geometry and velocity affect cone crack morphology and fracture mechanics?

Primary cone angles exhibit plateau behaviour within velocity regimes, with nested cone and secondary cone formation occurring beyond a critical threshold. Within regimes, velocity does not significantly control cone angle magnitude. Geometric parameters dominate cone crack nucleation and propagation behaviour. Inverse relationships are observed between primary cone angle and tile thickness ($\alpha_1 \propto -t_c$) and between secondary cone angle and secondary cone height ($\alpha_2 \propto -h_3$). Projectile size governs nucleation geometry, with $h_c \propto r_p$ and $r_1 \propto r_p$ across all materials. Surface roughness increases progressively along the cone flank, reflecting propagation complexity rather than velocity magnitude where the intermediate velocity regime appears to represent a transition from stable to unstable crack growth, as characterized from rapid amplification followed by stagnation.

The investigated fracture modes are statistically insensitive to geometric and velocity effects, although at elevated impact velocities local phenomenons are observed form near the comminuted zone, as visualized in Figure 22. These phenomenons are attributed to high impact pressures inducing inter- and intragranular shear of pulverized ceramic, with friction induced adiabatic regions causing transient melting from high enthalpy. Upon separation of the cone from the tile flash cooling of the melt yields observable remnants of solidified melt-deprived areas and clustered rippled ridges due to viscous surface adhesion, before recrystallization can occur. Amorphization and geometric analysis of the phenomenon are to be investigated in future research.

Thereby, velocity activates regime specific cone geometry and fracture behaviour, while tile geometry controls cone morphology, and nucleation mechanics are projectile geometry dependent.

RQ2 — How do intrinsic ceramic properties affect cone crack morphology and fracture mechanics?

Macroscopic cone morphology is not significantly distinguishable across Al_2O_3, SiC, and Si_3N_4 from the investigated specimens. Although magnitudes vary and are non-comparable for different thicknesses, geometric scaling trends are found to be consistent for the characterized material properties, with no indisputable and fundamentally grounded relationships between intrinsic ceramic properties and morphology or topology.

The investigated fracture mode regimes are identified and attributed to the ceramic material types, although an inexplicable inverse trend observed for transgranular fracture as a function of elastic modulus is observed, and no correlation is found for other investigated intrinsic material properties. A similar proportional increase has previously been reported[93], and is considered accepted in research. Investigation into the hypothesised melt phenomenon found in Al_2O_3 can be extended to different ceramics to identify differences in crack nucleation behaviour at high impact velocities.

To summarize, intrinsic ceramic properties have ample effect on geometric and topological cone crack factors, but are the dominant factor in determining fracture mode regimes.

RQ3 — Can sphere impact testing predict ballistic cone crack morphology and fracture mechanics?

The quantifiable and comparable macroscopic, mesoscopic, and microscopic characteristics investigated in this research are schematically visualized in Figure 30.

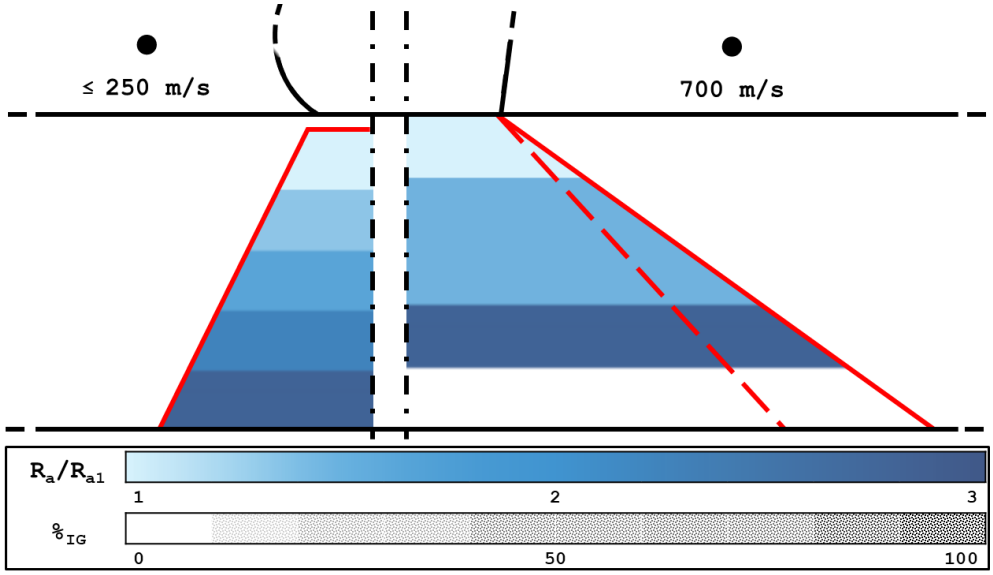

Figure 30: Schematic of Geometric (Red), Topological (Blue Gradient), and Fracture Mode (Hatched Density) Identified and Compared for Low Velocity Sphere Impact (left) and High Velocity Bullet Impact (right) of an Al_2O_3 Ceramic Tile, With Data From subsubsection 3.2.1,subsection 3.3, and subsection 3.4.

At the geometric macrostructure level, low-velocity sphere impacts yield smaller primary cone angles compared to high-velocity bullet impacts. However, intermediate- and high-velocity sphere impacts exhibit nested cone angles that can nucleate and propagate at magnitudes comparable to those computed from bullet impacts, indicating similar crack mechanics. Furthermore, cone angle scaling as a function of tile thickness is statistically correlatable for sphere impacts with similar trends observed for bullets, and nucleation geometry consistently scales with spherical projectile radius. This nucleation scaling remains to be quantified explicitly for bullet geometry, but comparable decoupling from geometric macrostructures suggest minimal effective influence of projectile geometry.

At the mesostructural level, surface topology trends for sphere impacts below 250 m/s and bullet impacts at 700 m/s display comparable progressive roughness amplification along the fracture surface, suggesting similar crack propagation mechanisms despite differences in absolute roughness magnitude. At the microstructural level, the identified fracture modes show no statistically significant deviation between impact methods for identical materials, yielding comparable relative proportions of intergranular and transgranular fracture.

These findings require validation through an increased statistical quantity of bullet impacts (n = 1), sphere testing at velocities beyond 700 m/s to assess crack propagation of greater cone angles, bullet testing at reduced velocities for assessing bi-directionality, rejection of coincidental tile thickness effects, and implementation of enhanced geometric characterization techniques for ballistic impacts.

To conclude, sphere impact testing provides a reliable geometric, topological, and fracture mode approximation of ballistic cone crack behaviour when investigated at multiple velocity regimes.

5 Conclusions and Recommendations

This work investigated the correlation between cone cracks formed by sphere impact and those formed under ballistic impact conditions across Al_2O_3, SiC, and Si_3N_4 ceramics. Macroscopic geometry, mesoscopic surface roughness, and microscopic fracture modes were quantified and statistically evaluated to identify relationships.

Three velocity regimes are researched: low ($\leq$ 250 m/s), intermediate (300–550 m/s), and high ($\geq$ 600 m/s), representing a common gas gun regime, a transition regime, and a regime representative for bullets. It was found that velocity primarily governs quantities and degrees of nested primary and secondary cone angle, with transition regimes, rather than a continuous evolution.

Geometric scaling relationships dominate cone morphology. In the intermediate regime, primary cone angle decreases proportionally with increasing tile thickness, and secondary cone angle decreases linearly with increasing secondary cone formation height. Projectile size governs cone crack nucleation geometry through proportional scaling of cone nucleation depth and truncated cone radius with projectile radius. These geometric relationships are found to be consistent for all investigated materials.

Surface roughness evolution shows progressive amplification along the cone propagation path for all ceramics and velocity regimes. While absolute roughness magnitudes increase for bullet impacts, normalized trends remain comparable, indicating geometry-controlled relative propagation mechanisms.

Material properties primarily influence relative areal occurrences of fracture modes. SiC exhibits predominantly transgranular fracture, Si_3N_4 predominantly intergranular fracture, and Al_2O_3 a mixed trans- and intergranular fracture modes. These fracture mode distributions remain largely independent of projectile velocity and geometry, and crack location, acknowledging the primary influence of intrinsic material properties.

Comparison between low velocity sphere and high velocity bullet impacts reveals analogous primary geometric regimes and trends when additional velocity and thickness sphere impacts are included, displays strong foundation for scaling of geometric relationships, and illustrates comparable ratios of fracture modes. Differences between impact types are increased fragmentation and subsequent limited distinguishment of fracture features under ballistic conditions rather than cone nucleation or propagation mechanics.

5.1 Recommendations

- Sphere impact test methods are no replacement for bullet testing of structural materials, but rather serve as a predictive screening method for novel materials and armour systems. Rapid testing cycles, reduced legal requirements, and enhanced postmortem characterization possibilities can be advantageous for research institutes, however the materials are to be rigorously tested and validated before being considered for ballistic protection.
- Significant intra-specimen variability of cone geometries highlight the degree of uncertainty of traditional characterization techniques. Three dimensional reconstruction and high speed video measurements yielded satisfactory certainty in this research, however further research efforts are recommended to focus on obtaining higher spatial and time resolution data, or developing alternative characterization techniques for improved reliability.
- In this research impact testing of bullets at decreased velocities ($\leq$600 m/s) are not completed, however experimental investigation of these conditions is advised to understand bi-directional correlatability of the presented trends and fits. The presented correlation is derived from free standing and unconstrained ceramic tiles, as these boundary conditions can affect the outcomes it is advised to translate the findings of this work into ceramics adhered to backings, or fully constrained tile test set-ups. Additionally, the range of materials and material properties investigated in this work are limited, and extensive research are to be focussed at broader range of (research) materials.
- An explanation for observed phenomenons near the impact site are hypothesized, but require experimental, numerical and analytical future research to build on the understanding high velocity impact mechanics.

References

[1] Abbas, MKG et al. "A state-of-the-art review on alumina toughened zirconia ceramic composites". In: *Materials Today Communications* 37 (2023), p. 106964.

[2] AEP, NATO Standard. "Multi-calibre manual of proof and inspection (M-CMOPI) for NATO small arms ammunition". In: *Edition A, Version* 1 (2020).

[3] Akimune, Y. "Hertzian cone crack in SiC caused by spherical particle impact". In: *Journal of materials science letters* 9.6 (1990), pp. 659–662.

[4] Atsma, Aaron J. *DIONYSOS FAMILY*. https://www.theoi.com/Olympios/DionysosFamily.html. The Theoi Project, 2017.

[5] *Ballistic Research — Elevate Ballistic & Energetic Testing: Integrated Lab Solutions for High Precision and Efficiency*. https://www.ballisticresearch.eu/.

[6] Bhanoo, Sindya N. "Remnants of an Ancient Kitchen Are Found in China". In: *The New York Times* (June 2021). URL: https://www.nytimes.com/2012/07/03/science/oldest-known-pottery-found-in-china.html (visited on 07/26/2024).

[7] Boussinesq, MJ. "Application des potentiels à l'étude de l'équilibre et du mouvement des solides élastiques: principalement au calcul des déformations et des pressions que produisent, dans ces solides, des efforts quelconques exercés sur une petite partie de leur surface ou de leur intérieur : mémoire suivi de notes étendues sur divers points de physique, mathematique et d'analyse." In: *(No Title)* (1885).

[8] Buffolo, M et al. "Review and outlook on GaN and SiC power devices: Industrial state-of-the-art, applications, and perspectives". In: *IEEE Transactions on Electron Devices* 71.3 (2024), pp. 1344–1355.

[9] Carton, Erik P et al. "Round robin using the depth of penetration test method on an armour grade alumina". In: *Defence Technology* 15.6 (2019), pp. 829–836.

[10] Chang, W et al. "Chemical vapor processing and applications for nanostructured ceramic powders and whiskers". In: *Nanostructured Materials* 4.5 (1994), pp. 507–520.

[11] Compton, Brett G., Gamble, Eleanor A., and Zok, Frank W. "Failure initiation during impact of metal spheres onto ceramic targets". In: *International Journal of Impact Engineering* 55 (2013), pp. 11–23.

[12] CoorsTek. *Ceramic Material Properties*. https://www.coorstek.com/media/4244/ceramic-material-properties.pdf. CoorsTek, n.d.

[13] Crary, John W. *Sixty Years a Brickmaker: A Practical Treatise on Brickmaking and Burning and the Management and Use of Different Kinds of Clays and Kilns for Burning Brick*. TA Randall & Company, 1890.

[14] Crookes, Robert G, März, Benjamin, and Wu, Houzheng. "Ductile deformation in alumina ceramics under quasi-static to dynamic contact impact". In: *Materials & Design* 187 (2020), p. 108360.

[15] Crouch, Ian G, Kesharaju, Manasa, and Nagarajah, Romesh. "Characterisation, significance and detection of manufacturing defects in Reaction Sintered Silicon Carbide armour materials". In: *Ceramics International* 41.9 (2015), pp. 11581–11591.

[16] Cui, Fengdan et al. "Effect of Ceramic Properties and Depth-of-penetration Test Parameters on the Ballistic Performance of Armour Ceramics." In: *Defence Science Journal* 67.3 (2017).

[17] Dadkhah, Mehran et al. "Additive manufacturing of ceramics: Advances, challenges, and outlook". In: *Journal of the European Ceramic Society* 43.15 (2023), pp. 6635–6664.

[18] Dancer, Claire E.J. et al. "High strain rate indentation-induced deformation in alumina ceramics measured by Cr3+ fluorescence mapping". In: *Journal of the European Ceramic Society* 31.13 (2011), pp. 2177–2187.

[19] Delfini, Andrea et al. "Advanced radar absorbing ceramic-based materials for multifunctional applications in space environment". In: *Materials* 11.9 (2018), p. 1730.

[20] Derevianko, Anatoly P et al. "AMS 14C age of the earliest pottery from the Russian Far East: 1996–2002 results". In: *Nuclear instruments and methods in physics research section B: Beam interactions with materials and atoms* 223 (2004), pp. 735–739.

[21] Deutsche Edelstahlwerke. *Prüfbericht QWP-Nr. 734/8*. Labor QWP – Krefeld, July 28, 2008.

[22] Duran, Cihangir et al. “Eco-friendly processing and methods for ceramic materials-A review”. In: *Journal of the Ceramic Society of Japan* 116.1359 (2008), pp. 1175–1181.

[23] Evers, Koen et al. “Nacre-like alumina with unique high strain rate capabilities”. In: *Journal of the European Ceramic Society* 40.2 (2020), pp. 417–426. ISSN: 0955-2219. DOI: https://doi.org/10.1016/j.jeurceramsoc.2019.09.015. URL: https://www.sciencedirect.com/science/article/pii/S0955221919306144.

[24] Federation, Russian. *GOST 34282–2017—Armored protection of vehicles*. 2017.

[25] Federation, Russian. *GOST 34286–2017—Armored clothing*. 2017.

[26] Field, JE, Sun, Q, and Townsend, D. “Ballistic impact of ceramics”. In: *Mechanical Properties of Materials at High Rates of Strain 1989* (1989), pp. 387–394.

[27] Fuller, ER Jr et al. “Toughening mechanisms in ceramic composites-semi-annual progress report for the period ending March 31, 1989”. In: (1989).

[28] Gadow, R and Jiménez, M. “Carbon fiber-reinforced carbon composites for aircraft brakes”. In: *Am. Ceram. Soc. Bull* 98.6 (2019), pp. 28–34.

[29] Gadow, Rainer and Von Niessen, Konstantin. “Lightweight ballistic with additional stab protection made of thermally sprayed ceramic and cermet coatings on aramide fabrics”. In: *International journal of applied ceramic technology* 3.4 (2006), pp. 284–292.

[30] Gooch, William A. “Overview of the development of ceramic armor technology: Past, present and the future”. In: *Ceramic Engineering and Science Proceedings*. Vol. 32. 5. 2011, pp. 195–213.

[31] Hausmann, Matthias, Klietz, Wenzel, and Garbes, Josef. *Method for purifying silicon carbide*. US Patent App. 17/626,062. Aug. 2022.

[32] Hazell, Paul J. *Armour: materials, theory, and design*. CRC press, 2022.

[33] Hojo, Junichi. *Materials chemistry of ceramics*. Springer, 2019.

[34] Hossain, Sk S and Roy, PK. “Sustainable ceramics derived from solid wastes: a review”. In: *Journal of Asian Ceramic Societies* 8.4 (2020), pp. 984–1009.

[35] Iperen, Jolanda van et al. “The White Glaze of Delft Blue: A Comparative Study of Historical Recipes for the White Tin Glaze Used in Delftware and Other Dutch Tin-glazed Earthenware During Their Heyday (c. 1600–1800)”. In: *Studies in Conservation* 70.3 (2025), pp. 187–204.

[36] Jakobsen, Martin Fonnum. *Cracking mechanisms in ceramic armor–analytical solutions and finite element simulations*. 2023.

[37] JUSTICE, NATIONAL INSTITUTE OF. *Ballistic Resistance of Body Armor NIJ Standard–0101.06*. https://www.nist.gov/system/files/documents/oles/ballistic.pdf. July 2008.

[38] Kaufmann, Christian et al. “Influence of material properties on the ballistic performance of ceramics for personal body armour”. In: *Shock and Vibration* 10.1 (2003), pp. 51–58.

[39] Kedir, Nesredin. “In situ characterization of damage kinetics during foreign object debris (FOD) impact of silicon carbide”. PhD thesis. Purdue University, 2021.

[40] Khan, MK et al. “An investigation of the ballistic performance of independent ceramic target”. In: *Thin-Walled Structures* 154 (2020), p. 106784.

[41] Kobylkin, IF. “Mechanics of penetration of ceramic targets”. In: *Combustion, Explosion, and Shock Waves* 53.1 (2017), pp. 110–115.

[42] Krenkel, Walter and Langhof, Nico. “Ceramic matrix composites for high performance friction applications”. In: *Proceedings of the IV advanced ceramics and applications conference*. Springer. 2017, pp. 13–28.

[43] Kumar, Sourabh and Le Ferrand, Hortense. “Nacre-like ceramic–metal composites: State-of-the-art, challenges, and opportunities”. In: *Journal of the American Ceramic Society* (2025), e20623.

[44] Lapini, Pietro. “Failure and Damage Modelling of Alumina in Ceramic-Composite Ballistic Protection”. PhD thesis. Politecnico di Torino, 2025.

[45] Le Losq, Charles et al. “Silicate glasses”. In: *Springer handbook of glass*. Springer, 2019, pp. 441–503.

[46] Leavy, R Brian, Brannon, Rebecca M, and Strack, O Erik. “The use of sphere indentation experiments to characterize ceramic damage models”. In: *International Journal of Applied Ceramic Technology* 7.5 (2010), pp. 606–615.

[47] Lee, Sang-Kee et al. "Crack-healing behavior and resultant strength properties of silicon carbide ceramic". In: *Journal of the European Ceramic Society* 25.5 (2005), pp. 569–576.

[48] Ma, Minghui et al. "Crack propagation and energy absorption of thin ceramic plate under impact". In: *Ceramics International* (2025).

[49] Mahajan and Luby. *Handbook of Advanced Ceramics and Composites*. Springer International Publishing, 2020.

[50] Meyers, Marc André and Chawla, Krishan Kumar. *Mechanical behavior of materials*. Cambridge university press, 2008.

[51] Milak, Pâmela et al. "The influence of dopants in the grain size of alumina-a review". In: *Materials Science Forum*. Vol. 820. Trans Tech Publ. 2015, pp. 280–284.

[52] Miller, Robert A. "Thermal barrier coatings for aircraft engines: history and directions". In: *Journal of thermal spray technology* 6.1 (1997), pp. 35–42.

[53] Mouginot, R and Maugis, D. "Fracture indentation beneath flat and spherical punches". In: *Journal of materials science* 20.12 (1985), pp. 4354–4376.

[54] Moynihan, Thomas J, Chou, Shun-Chin, and Mihalcin, Audreyk L. *Application of the depth-of-penetration test methodology to characterize ceramics for personnel protection*. Tech. rep. 2000.

[55] Mukhtar, Masood et al. "Toughening of alumina ceramics by nanograin refinement". In: *Ceramics International* (2025).

[56] NATO, (NSO) STANDARDIZATION OFFICE. *AEP-97 - MULTI-CALIBRE MANUAL OF PROOF AND INSPECTION (M-CMOPI) FOR NATO SMALL ARMS AMMUNITION*. https://diweb.hq.nato.int/naag/Pages/Public-Release-Documents.aspx. NATO Army Armaments Group (NAAG), Okt 2020.

[57] Niihara, K. "A fracture mechanics analysis of indentation-induced Palmqvist crack in ceramics". In: *Journal of materials science letters* 2.5 (1983), pp. 221–223.

[58] Oh, Sang Yeob and Shin, Hyung Seop. "Effect of particle impact velocity on cone crack shape in ceramic material". In: *Key Engineering Materials* 297 (2005), pp. 1321–1326.

[59] Pelleg, Joshua. *Mechanical properties of materials*. Vol. 190. Springer, 2013.

[60] Rahaman, Mohamed N. *Ceramic processing and sintering (2nd ed)*. CRC press, 2017.

[61] Rice, Prudence M. *Pottery analysis: a sourcebook*. University of Chicago press, 2015. Chap. Pottery and Its History, pp. 3–32.

[62] Ritchie, Robert O. "Toughening materials: enhancing resistance to fracture". In: *Philosophical Transactions of the Royal Society A* 379.2203 (2021), p. 20200437.

[63] Rizzo, Antonella et al. "The critical raw materials in cutting tools for machining applications: A review". In: *Materials* 13.6 (2020), p. 1377.

[64] Rozenberg, Z and Yeshurun, Y. "The relation between ballastic efficiency and compressive strength of ceramic tiles". In: *International journal of impact engineering* 7.3 (1988), pp. 357–362.

[65] Sabzi, M et al. "A review on sustainable manufacturing of ceramic-based thin films by chemical vapor deposition (CVD): reactions kinetics and the deposition mechanisms". In: *Coatings* 13.1 (2023), p. 188.

[66] Shivakumar, Sujai, Yoon, Julia, and Sirkar, Tisyaketu. "Gallium Nitride: A Strategic Opportunity for the Semiconductor Industry". In: *Center for Strategic & International Studies* (May 2024). URL: https://www.csis.org/analysis/gallium-nitride-strategic-opportunity-semiconductor-industry (visited on 07/26/2024).

[67] Silveira, PHPMD et al. "A brief review of alumina, silicon carbide and boron carbide ceramic materials for ballistic applications". In: *Academia Letters* 3742 (2021), pp. 1–11.

[68] Simons, Erik. "Ceramic material under ballistic loading: A numerical approach to sphere impact on ceramic armour material". In: (2020).

[69] STANAG, NATO. "4569: protection levels for occupants of armoured vehicles". In: NATO RTO. 2004.

[70] STANDARDS, BUREAU OF INDIAN. *IS 17051 2018 -Textiles — bullet resistant jackets — performance requirements.* 2018. URL: https://www.mha.gov.in/sites/default/files/2023-03/BRJ_09032023.pdf.

[71] Steinbrech, RW. "Toughening mechanisms for ceramic materials". In: *Journal of the European Ceramic Society* 10.3 (1992), pp. 131–142.

[72] Takahashi, Manabu et al. "Estimation of foreign-object damage to silicon carbide plates by silicon nitride spherical projectiles". In: *Procedia materials science* 3 (2014), pp. 83–89.

[73] Testing, American Society for and Advanced Ceramics, Materials. Committee C28 on. *ASTM C1322-15, Standard practice for fractography and characterization of fracture origins in advanced ceramics*. ASTM International, 2019.

[74] Testing, American Society for and Advanced Ceramics, Materials. Committee C28 on. *ASTM C1327-15, Standard Test Method for Vickers Indentation Hardness of Advanced Ceramics*. ASTM International, 2015.

[75] Testing, American Society for and Advanced Ceramics, Materials. Committee C28 on. *ASTM E112-10, Standard Test Method for Determining Average Grain Size*. ASTM International, 2010.

[76] Testing, American Society for and Advanced Ceramics, Materials. Committee C28 on. *ASTM E140-23, Standard Hardness Conversion Tables for Metals: Relationship Among Brinell Hardness, Vickers Hardness, Rockwell Hardness, Superficial Hardness, Knoop Hardness, and Scleroscope Hardness*. 2019.

[77] Testing, American Society for and Advanced Ceramics, Materials. Committee C28 on. *ASTM E1508-12a, Standard Guide for Quantitative Analysis by Energy-Dispersive Spectroscopy*. 2019.

[78] Testing, American Society for and Advanced Ceramics, Materials. Committee C28 on. *ASTM E494-20, Standard Practice for Measuring Ultrasonic Velocity in Materials by Comparative Pulse-Echo Method*. ASTM International, 2025.

[79] Tokita, Masao. "Progress of spark plasma sintering (SPS) method, systems, ceramics applications and industrialization". In: *Ceramics* 4.2 (2021), pp. 160–198.

[80] Toussaint, Geneviève and Polyzois, Ioannis. "Steel spheres impact on alumina ceramic tiles: Experiments and finite element simulations". In: *International Journal of Applied Ceramic Technology* 16.6 (2019), pp. 2131–2152.

[81] Van der Zwaag, S. "Routes and mechanisms towards self healing behaviour in engineering materials". In: *Bulletin of the polish academy of sciences Technical sciences* (2010), pp. 227–236.

[82] Verbeek, Adriaan Thomas Jacques. "Plasma sprayed thermal barrier coatings: production, characterization and testing". In: (1992).

[83] Wade, James. "Contact damage of ceramics and ceramic nanocomposites". PhD thesis. Loughborough University, 2017.

[84] Wang, Shuai et al. "Recycling B4C grinding waste to fabricate high-performance ceramics by modification treatments and hot pressing". In: *Journal of Environmental Management* 371 (2024), p. 123230.

[85] Wang, Zhiyong. "On the characterization of mechanical properties of alumina ceramics for high speed application". PhD thesis. 2015.

[86] Wei, Zhijun, Yu, Tao, and An, Yumin. "Research progress on impact resistance properties of fiber-reinforced ceramic matrix composites". In: *Journal of Physics: Conference Series*. Vol. 3080. 1. IOP Publishing. 2025, p. 012131.

[87] Wilkins, Mark, Honodel, Charles, and Sawle, David. *APPROACH TO THE STUDY OF LIGHT ARMOR*. Tech. rep. California Univ., Livermore. Lawrence Radiation Lab., 1967.

[88] Wilkins, ML, Cline, CF, and Honodel, CA. *Fourth progress report of light armor program*. Tech. rep. California Univ., Livermore. Lawrence Radiation Lab., 1969.

[89] Woodward, RL and Baxter, BJ. "Ballistic evaluation of ceramics: influence of test conditions". In: *International journal of impact engineering* 15.2 (1994), pp. 119–124.

[90] Woodward, RL et al. "A study of fragmentation in the ballistic impact of ceramics". In: *International Journal of Impact Engineering* 15.5 (1994), pp. 605–618.

[91] Woolsey, Patrick, Kokidko, David, and Mariano, Stephen A. *Alternative test methodology for ballistic performance ranking of armor ceramics*. Tech. rep. 1989.

[92] Wu, Houzheng et al. "Ballistic Damage of Alumina Ceramics-Learning from Fragments". In: *Advances in Ceramic Armor X: A Collection of Papers Presented at the 38th International Conference on Advanced Ceramics and Composites January 27–31, 2014*. Vol. 35. Wiley Online Library. 2014, pp. 49–62.

[93] Yamada, Masayoshi et al. “Relationship between the cone crack and fracture mode in ceramics under high-velocity-projectile impact”. In: *Journal of the Ceramic Society of Japan* 118.1382 (2010), pp. 903–908.

[94] Yang, Shanglin et al. “Experimental and theoretical study of cone angle in alumina tiles under ballistic impact”. In: *International Journal of Impact Engineering* 192 (2024), p. 105025.

[95] Yoffe, EH. “Elastic stress fields caused by indenting brittle materials”. In: *Philosophical Magazine A* 46.4 (1982), pp. 617–628.

[96] Yuan, JC et al. “Cone cracking and fragmentation of alumina plates under high-speed penetration: Experiments and modeling”. In: *Engineering Fracture Mechanics* 314 (2025), p. 110733.

Appendices

A Literature Research

A.a Relationship Between Cone Angle and Cone Volume

$$V = \tfrac{1}{3}\pi h\,(R^2 + Rr + r^2), \qquad \tan(\alpha) = \frac{R-r}{h}.$$

$$\frac{3V}{\pi h} = R^2 + Rr + r^2,$$

$$R^2 + rR + \left(r^2 - \frac{3V}{\pi h}\right) = 0,$$

$$R = \frac{-r \pm \sqrt{-3r^2 + \frac{12V}{\pi h}}}{2},$$

$$R - r = \frac{-3r \pm \sqrt{\frac{12V}{\pi h} - 3r^2}}{2},$$

$$\tan(\alpha) = \frac{R-r}{h} = \frac{-3r \pm \sqrt{\frac{12V}{\pi h} - 3r^2}}{2h}.$$

A.b Stress Tensors and Crack Direction

$$\begin{aligned}\sigma_r =& \frac{3P}{2\pi a^2}\left[\frac{1-2\nu}{3}\frac{a^2}{r^2}\left(1 - \frac{z^3}{u^{3/2}}\right) + \frac{z^3a^2}{u^{3/2}(u^2+a^2z^2)}\right.\\ &\left. + \frac{z}{\sqrt{u}}\left(\frac{(1-\nu)u}{a^2+u} + (1+\nu)\frac{\sqrt{u}}{a}\tan^{-1}\left(\frac{a}{\sqrt{u}}\right) - 2\right)\right]\\ &+ \frac{2B}{R^3}\left[2(1-2\nu) - \frac{3}{R^2}\left(z^2(1-2\nu) + 2r^2(1-\nu) - \frac{15z^2r^2}{R^2}\right)\right]\end{aligned} \tag{12}$$

$$\begin{aligned}\sigma_\phi =& \frac{3P}{2\pi a^2}\left[\frac{1-2\nu}{3}\frac{a^2}{r^2}\left(1 - \frac{z^3}{u^{3/2}}\right) - \frac{z}{\sqrt{u}}\left(\frac{(1-\nu)u}{a^2+u} + (1+\nu)\frac{\sqrt{u}}{a}\tan^{-1}\left(\frac{a}{\sqrt{u}}\right)\right)\right]\\ &+ \frac{2B}{R^3}\left[2(1-2\nu) - \frac{3}{R^2}\left(z^2(1-2\nu) + r^2(1-\nu)\right)\right]\end{aligned} \tag{13}$$

$$\begin{aligned}\sigma_z =& \frac{3P}{2\pi a^2}\left[\frac{z^3}{u^{3/2}}\right]\\ &+ \frac{2B}{R^3}\left[2(1-2\nu) - \frac{3z^2}{R^2}\right]\end{aligned} \tag{14}$$

$$\begin{aligned}\tau_{rz} =& -\frac{3P}{2\pi a^2}\left[\frac{rz^2}{u^{3/2}}\right]\\ &- \frac{2B}{R^3}\left[\frac{3rz}{R^2}\right]\end{aligned} \tag{15}$$

A.c Impact Testing Formulas

Vicker's and Brinell hardness and Fracture Toughness are calculated from:

$$HV = \frac{1.8544\,P}{d^2} \tag{16}$$

$$H_B = \frac{2P}{\pi D\left(D - \sqrt{D^2 - d^2}\right)} \tag{17}$$

$$K_{IC} = 0.016\left(\frac{E}{H}\right)^{1/2}\frac{P}{c^{3/2}} \tag{18}$$

. where P is the applied load and d is the average indentation diameter.

$$BE = \frac{\rho_b(p_{b,0} - p_{b,c})}{\rho_c t_c^*} \tag{19}$$

where:

- BE is the ballistic efficiency factor,
- ρ_b is the density of the backing,
- ρ_c is the density of the ceramic,
- $p_{b,0}$ is the penetration depth into the bare backing,
- $p_{b,c}$ is the penetration depth into the backing with ceramic,
- t_c^* is the ceramic thickness,

$$U_{abs} = U_{frac} + U_{frag} + U_{acc} = \frac{1}{2}M_p({v_p}^2 - {v_p^*}^2) - \frac{1}{2}M_c v_c^2 \tag{20}$$

where:

- U_{abs} is the absolute energy dissipation,
- U_{frac} is the energy dissipated through ceramic fracture,
- U_{frag} is the kinetic energy carried by ejected fragments,
- U_{acc} is the cone acceleration energy,
- M_p is the projectile mass,
- M_c is the cone mass,
- v_p is the impact velocity,
- v_p^* is the residual velocity of projectile core and cone,

B Material Characterization

- **Geometry, Mass and Density**
  - Tile mass: digital scale (±1 mg $\leq$ 100 g, ±1 g $\geq$ 100 g)
  - Projectile mass: digital scale (±0.1 mg), mean of 10
  - Tile thickness: digital micrometer (±1 μm), 5 locations
  - Tile length/width: mechanical caliper (±10 μm), 3 locations
  - Projectile diameter: digital caliper (±1 μm), mean of 10
  - Density: $\rho = m/V$, for Tile: $V = lwt$ or Sphere: $V = \frac{\pi}{6} d_p^3$

Elastic Properties (Ultrasonic Pulse-Echo)

- ±10 MHz longitudinal and transverse transducers
- Oscilloscope: WaveSurfer 4034HD (5 MHz)
- Manual alignment of reflection time τ_r and number of reflections N_r
- Sound velocities: $v = 2tN_r/\tau_r$
- Elastic constants (E, G, B, ν) from isotropic relations using ρ, v_L, v_T

Specimen Preparation (Hardness & Microstructure)

- $\sim$10 mm specimens cut (diamond saw) or retrieved from fragments
- Embedded in glass fibre–filled resin
- Ground, polished, cleaned with isopropyl alcohol

Hardness and Indentation Fracture Toughness

- Microhardness tester: InnovaTest FALCON 500 (Vickers)
- Indenter: 136° diamond
- Load: 1 kgf, dwell time: 10 s
- 10 indents per specimen (ASTM C1327)
- Optical measurement: ×40 (ceramic), ×10 (projectiles)
- Hardness: $HV = 1.8544 \dfrac{4P}{(d_{HV,H} + d_{HV,V})^2}$
- Fracture toughness: $K_{IC} = 0.016 \left(\dfrac{E}{HV}\right)^{1/2} \dfrac{P}{c_{HV}^{3/2}}$

Microstructure (SEM & Grain Size)

- Gold coating: 15 nm (plasma deposited)
- SEM: JEOL JSM-7500
- 15 kV, 20 μA, 20 ± 0.1 mm working distance
- Magnifications: ×25, ×100, ×500, ×2000, ×5000
- EDS area measurements (atomic wt.%)
- Grain size: ASTM E112 intercept method
  - 5 horizontal + 5 vertical lines per image ($\geq$ ×500)

  - Mean intercept: $\bar{l} = L_T/N_i$

- **Digital Optical Microscope — OLYMPUS DSX-1000**
  - Tiles: 1× objective, 1.4× zoom, 10% overlap, oblique lighting
  - Image size: 1210 × 1210 px (13 450 × 13 450 μm)
  - Lateral resolution: 11.1 μm/px
  - Vertical pitch: 243 μm
  - Vertical resolution: 30 μm
  - 3D stitching and digital focus analysis
- **Digital Optical Microscope — OLYMPUS LEXT OLS5000 (v1.3 / v1.3.4.320)**
  - Cones: 10× objective, 1× zoom, 10–20% overlap
  - Bright-field or oblique lighting
  - Image size: 1210 × 1210 px (1940 × 1940 μm)
  - Lateral resolution: 1.59 μm/px
  - Vertical pitch: 43 μm
  - Vertical resolution: 3 μm
  - 3D reconstruction and morphology analysis
- **High-Speed Camera — Shimadzu HyperVision HPV-2**
  - Frame rate: 500,000 fps
  - 101 frames (200 μs time window)
  - Resolution: 312 × 260 px
  - Field of view: ≈100 × 83 mm
  - Spatial resolution: 0.323 mm/px
  - Analysis: Tracker Video Analysis, GNU Octave 10.3.0
- **Scanning Electron Microscope — JEOL JSM-7500**
  - Gold coating: 15 nm (plasma deposited)
  - Accelerating voltage: 15 kV
  - Beam current: 20 μA
  - Working distance: 20 ± 0.1 mm
  - Magnifications: ×25, ×100, ×500, ×2000, ×5000

3 Results

Table 13: Regression results for α_1 as a function of v_p

α_1 Regime	Fitted Regression	n	b_0	b_1	b_2	b_3	R2	RMSE	p
	$\alpha_1 = b_0$	16	42.350	-	-	-	0.000	3.327	1.000
35 – 50	$\alpha_1 = b_0 + b_1\,x$	16	43.345	-0.00249	-	-	0.010	3.310	0.708
	$\alpha_1 = b_0 + b_1\,x + b_2\,x^2$	16	56.798	-0.07352	8.381e-05	-	0.417	2.541	0.030
	$\alpha_1 = b_0$	5	58.192	-	-	-	0.000	1.529	1.000
50 – 65	$\alpha_1 = b_0 + b_1\,x$	5	53.969	0.00706	-	-	0.227	1.345	0.417
	$\alpha_1 = b_0 + b_1\,x + b_2\,x^2$	5	125.180	-0.24945	2.232e-04	-	0.835	0.621	0.165
	$\alpha_1 = b_0$	1	72.354	-	-	-	NaN	0.000	NaN
65 – 80	$\alpha_1 = b_0 + b_1\,x$	1	0.000148	0.10336	-	-	-Inf	0.000	NaN
	$\alpha_1 = b_0 + b_1\,x + b_2\,x^2$	1	NaN	NaN	NaN	-	NaN	NaN	NaN

Table 14: Regression results for α_2 as a function of v_p

α_2 Regime	Fitted Regression	n	b_0	b_1	b_2	b_3	R2	RMSE	p
	$\alpha_2 = b_0$	17	67.022	-	-	-	0.000	2.927	1.000
55 – 75	$\alpha_2 = b_0 + b_1\,x$	17	62.555	0.00937	-	-	0.137	2.719	0.144
	$\alpha_2 = b_0 + b_1\,x + b_2\,x^2$	17	61.482	0.01371	-4.156e-06	-	0.137	2.719	0.356

Table 15: Regression results for R_a as a function of Crack Propagation

v_p regime	Fitted Regression	n	b_0	b_1	b_2	b_3	R2	RMSE	p
	$R_a = b_0$	65	1.839	-	-	-	0.000	1.154	1.000
$\leq$250	$R_a = b_0 + b_1 x$	65	0.604	0.412	-	-	0.255	0.997	1.83e-05
	$R_a = b_0 + b_1 x + b_2 x^2$	65	0.583	0.430	-0.00298	-	0.255	0.997	1.11e-04
	$R_a = b_0$	85	1.803	-	-	-	0.000	0.732	1.000
300-550	$R_a = b_0 + b_1 x$	85	0.908	0.298	-	-	0.332	0.599	8.00e-09
	$R_a = b_0 + b_1 x + b_2 x^2$	85	0.297	0.822	-0.0873	-	0.372	0.580	5.32e-09
	$R_a = b_0$	24	1.486	-	-	-	0.000	0.514	1.000
$\geq$600	$R_a = b_0 + b_1 x$	24	1.145	0.117	-	-	0.099	0.487	0.134
	$R_a = b_0 + b_1 x + b_2 x^2$	24	0.271	0.874	-0.128	-	0.269	0.439	0.0373

Table 16: Regression results for α_1 as a function of t_c and α_2 as a function of h_3

v_p regime	Fitted Regression	n	b_0	b_1	b_2	b_3	R2	RMSE	p
≤250	$\alpha_1 = b_0$	13	48.133	-	-	-	0.000	1.996	1.000
	$\alpha_1 = b_0 + b_1 x$	13	56.564	-1.037	-	-	0.224	1.759	0.103
	$\alpha_1 = b_0 + b_1 x + b_2 x^2$	13	-28.522	19.269	-1.195	-	0.375	1.578	0.095
	$\alpha(t_c) = b_0 + b_1 \tan\left(\frac{b_3}{2x}\, b_3\right)$	13	3.229	-	-	10.000	0.465	3.096	-
	$\alpha_2 = b_0$	2	73.022	-	-	-	0.000	4.063	1.000
	$\alpha_2 = b_0 + b_1 x$	1	10.432	24.709	-	-	-Inf	0.000	NaN
	$\alpha_2 = b_0 + b_1 x + b_2 x^2$	1	NaN	NaN	NaN	-	NaN	NaN	NaN
300-550	$\alpha_1 = b_0$	17	41.248	-	-	-	0.000	7.004	1.000
	$\alpha_1 = b_0 + b_1 x$	17	64.896	-2.190	-	-	0.312	5.811	0.020
	$\alpha_1 = b_0 + b_1 x + b_2 x^2$	17	-116.149	29.223	-1.320	-	0.324	5.760	0.065
	$\alpha(t_c) = b_0 + b_1 \tan\left(\frac{b_3}{2x}\, b_3\right)$	17	2.694	-	-	10-	0.300	4.392	-
	$\alpha_2 = b_0$	17	63.156	-	-	-	0.000	6.982	1.000
	$\alpha_2 = b_0 + b_1 x$	17	73.853	-3.838	-	-	0.706	3.787	2.43e-05
	$\alpha_2 = b_0 + b_1 x + b_2 x^2$	17	66.249	1.647	-0.761	-	0.785	3.239	2.13e-05
≥600	$\alpha_1 = b_0$	8	58.714	-	-	-	0.000	9.929	1.000
	$\alpha_1 = b_0 + b_1 x$	8	54.427	0.379	-	-	0.016	9.847	0.762
	$\alpha_1 = b_0 + b_1 x + b_2 x^2$	8	-149.555	31.203	-1.040	-	0.399	7.700	0.281
	$\alpha(t_c) = b_0 + b_1 \tan\left(\frac{b_3}{2x}\, b_3\right)$	8	10.790	-	-	10	-0.178	10.649	-
	$\alpha_2 = b_0$	4	68.593	-	-	-	0.000	2.456	1.000
	$\alpha_2 = b_0 + b_1 x$	2	16.521	29.405	-	-	0.000	1.841	NaN
	$\alpha_2 = b_0 + b_1 x + b_2 x^2$	2	NaN	NaN	NaN	-	NaN	NaN	NaN

Table 17: Regression results for $\%_{IG}$ as a function of Crack Propagation

Velocity Regime	Fitted Regression	n	b_0	b_1	b_2	b_3	R2	RMSE	p
≤ 250	$y = b_0$	7	0.3803	-	-	-	0.000	0.04752	1.000
	$y = b_0 + b_1 x$	7	0.4412	-0.02241	-	-	0.427	0.03599	0.112
	$y = b_0 + b_1 x + b_2 x^2$	7	0.3165	0.09238	-0.02013	-	0.960	0.00950	0.00160
343 - 550	$y = b_0$	13	0.4128	-	-	-	0.000	0.07793	1.000
	$y = b_0 + b_1 x$	13	0.4928	-0.02665	-	-	0.252	0.06740	0.0805
	$y = b_0 + b_1 x + b_2 x^2$	13	0.4507	0.01022	-0.00615	-	0.271	0.06654	0.206
≥600	$y = b_0$	13	0.4121	-	-	-	0.000	0.1003	1.000
	$y = b_0 + b_1 x$	13	0.3458	0.02210	-	-	0.105	0.09487	0.281
	$y = b_0 + b_1 x + b_2 x^2$	13	0.3430	0.02456	-0.000410	-	0.105	0.09487	0.575

Table 18: Regression results for R_a as a function of Crack Propagation for SiC

v_p	Fitted Regression	n	b_0	b_1	b_2	b_3	R2	RMSE	p
≤ 250)	$R_a = b_0$	35	1.727	-	-	-	0.000	0.812	1.000
	$R_a = b_0 + b_1 x$	35	0.609	0.373	-	-	0.422	0.618	2.45e-05
	$R_a = b_0 + b_1 x + b_2 x^2$	35	0.779	0.227	0.02436	-	0.424	0.616	1.46e-04